


5-2012

Use of Ultra High Vacuum Plasma Enhanced Chemical Vapor Deposition for Graphene Fabrication

Shannen Adcock

University of Arkansas, Fayetteville

Follow this and additional works at: <http://scholarworks.uark.edu/etd>

 Part of the [Condensed Matter Physics Commons](#), [Nanoscience and Nanotechnology Commons](#),
and the [Nanotechnology Fabrication Commons](#)

Recommended Citation

Adcock, Shannen, "Use of Ultra High Vacuum Plasma Enhanced Chemical Vapor Deposition for Graphene Fabrication" (2012).
Theses and Dissertations. 361.
<http://scholarworks.uark.edu/etd/361>

This Thesis is brought to you for free and open access by ScholarWorks@UARK. It has been accepted for inclusion in Theses and Dissertations by an authorized administrator of ScholarWorks@UARK. For more information, please contact scholar@uark.edu, ccmiddle@uark.edu.

USE OF ULTRA HIGH VACUUM PLASMA ENHANCED CHEMICAL VAPOR
DEPOSITION FOR GRAPHENE FABRICATION

USE OF ULTRA HIGH VACUUM PLASMA ENHANCED CHEMICAL VAPOR
DEPOSITION FOR GRAPHENE FABRICATION

A thesis submitted in partial fulfillment
of the requirements for the degree of
Master of Science in Electrical Engineering

By

Shannen Adcock
University of Arkansas
Bachelor of Science in Electrical Engineering, 2010

May 2012
University of Arkansas

Abstract

Graphene, what some are terming the “new silicon”, has the possibility of revolutionizing technology through nanoscale design processes. Fabrication of graphene for device processing is limited largely by the temperatures used in conventional deposition. High temperatures are detrimental to device design where many different materials may be present. For this reason, graphene synthesis at low temperatures using plasma-enhanced chemical vapor deposition is the subject of much research. In this thesis, a tool for ultra-high vacuum plasma-enhanced chemical vapor deposition (UHV-PECVD) and accompanying subsystems, such as control systems and alarms, are designed and implemented to be used in future graphene growths. Also in this thesis, a method to fabricate graphene using plasma-enhanced chemical vapor deposition is proposed and executed on a single-chamber chemical vapor deposition system. The as-grown films were studied using spectroscopic and microscopic techniques.

Analysis of the grown films indicated nanoscale, multilayer flake-like structures. The structures grown were crystalline and of uniform diameter. Energy-dispersive X-ray spectroscopy confirmed the main element of the flakes to be carbon. Though large-area graphene was not achieved, it is evident from this research that fine-tuning the parameters in the growth process would increase the possibility of monolithic graphene growth at low temperatures. The new UHV-PECVD system, with its cutting-edge capabilities, could be used to further research on graphene growth.

This thesis is approved for recommendation
to the Graduate Council.

Thesis Director:

Dr. Hameed Naseem

Thesis Committee:

Dr. Shui-Qing Yu

Dr. Samir El-Ghazaly

Thesis Duplication Release

I hereby authorize the University of Arkansas Libraries to duplicate this thesis when needed for research and/or scholarship.

Agreed _____
Shannen Adcock

Refused _____
Shannen Adcock

Acknowledgements

I would like to thank my advisor Dr. Hameed Naseem for allowing me the chance to work with him and his world-class team. The knowledge and experience Dr. Naseem has imparted to me is the most valuable I have received in my academic career thus far. I would also like to thank Dr. Fisher Yu for his continuous guidance in my work. Furthermore, thank you to Dr. Samir El-Ghazaly for his support and encouragement.

This research is financially supported by the University of Arkansas and Army Research Office DURIP program, Grant #W911NF101026. It was also funded by the Army Research Laboratory under Cooperative Agreement Number W911NF-10-2-0072 and W911NF-10-2-0093. Any opinions, findings, and conclusions or recommendations expressed in this thesis are those of the author and do not necessarily reflect the views of the University of Arkansas, Army Research Office, or Army Research Laboratory. The opportunity these funding agencies have provided to me is priceless.

Thank you to Dr. Husam Abu-Safe for his gracious help and support throughout my project. I would also like to thank Benjamin Conley, Aboozar Mosleh, Bryant Hankton, and Dr. Zafar Waqar for their hard work and unwavering support on the UHV-PECVD system. It has truly been an honor to work with such a fine team of students and other research personnel.

Finally, I would like to thank my mother and father for their encouragement, support, and advice throughout my entire academic career. Thank you to my brothers, Nick and Eric, for constantly serving as my inspiration to push myself harder than anyone else can push me. I would also like to thank my best friends Misty, Hannah, and Isabella – good friends are like stars; though you can't always see them, you know they're always there.

Table of Contents

Abstract	ii
Thesis Duplication Release.....	iv
Acknowledgements.....	v
Table of Contents	vi
List of Figures	viii
List of Tables	xi
Chapter 1: Introduction	1
Chapter 2: Graphene, the New Silicon	3
2.1: Characteristics of Graphene.....	3
2.2: Chemical Vapor Deposition of Graphene.....	4
2.3: Characterization Methods	6
2.3.1: Raman Spectroscopy.....	7
2.3.2: Electron Microscopy.....	9
2.3.3: Optical Transmittance	11
2.4: Summary of Graphene Literature Survey	11
2.4.1: First Isolation of Graphene	11
2.4.2: Thermally-Induced Growth	12
2.4.3: Plasma-Enhanced Growth.....	15
2.5: Outline of Research Goals and Objectives	24
Chapter 3: Experimental Methods	25
3.1: The UHV-PECVD System	25
3.1.1: Design of the UHV-PECVD System	28

3.1.2: Design of Control Systems	31
3.1.3: Safety Features.....	39
3.1.4: Status of the UHV-PECVD System.....	44
3.2: Overview of Single-Chamber CVD System.....	45
3.3: Experimental Procedures	46
Chapter 4: Results and Discussion.....	50
4.1: Results of Optical Transmittance.....	53
4.2: Results of Raman Spectroscopy	57
4.3: Results of Scanning Electron Microscopy.....	66
4.4: Results of Transmission Electron Microscopy	67
Chapter 5: Conclusion and Future Work	73
References.....	76

List of Figures

Figure 1: The graphene lattice and other carbon formations [2].	4
Figure 2: Comparison of Raman signal for bulk graphite and graphene [13].	9
Figure 3: Diagram of scanning electron microscopy imaging mechanism [15].	10
Figure 4: Diagram of transmission electron microscopy imaging mechanism [17].	11
Figure 5: Growth mechanism of thermal CVD [5].	13
Figure 6: Diagram of the UHV-PECVD System [38].	29
Figure 7: Diagram of solenoid on/off switching mechanism.	32
Figure 8: Photograph of main switchbox layout.	33
Figure 9: Map of main switchbox layout with valve numbers shown.	33
Figure 10: LabVIEW program Solenoid Control.vi user interface.	36
Figure 11: Schematic of the power supply switchbox.	37
Figure 12: Diagram showing signal progression from control schemes.	37
Figure 13: Image of the solenoid signal junction box.	38
Figure 14: Connections inside the solenoid signal junction box wiring diagram.	38
Figure 15: Image of the sniffer and alarm box.	41
Figure 16: Connections inside the sniffer alarm box.	41
Figure 17: Image of the high-pressure pneumatic junction box.	42
Figure 18: Connections inside the high pressure pneumatic junction box.	42
Figure 19: Image of the exhaust monitoring box.	43
Figure 20: Connections inside the exhaust monitoring box.	44
Figure 21: The single-chamber CVD system in room 350B of the ENRC.	45
Figure 22: Schematic of the single-chamber CVD system [46].	46

Figure 23: Nickel TEM grid (left) and TEM grid holder used in growth process.....	48
Figure 24: Image of deposition on copper substrates.	51
Figure 25: Image of deposition on nickel substrates.	51
Figure 26: Image of deposition on silicon substrates.....	52
Figure 27: Image of deposition on glass substrates.	52
Figure 28: Transmittance of samples grown at 280°C for 1, 5, and 10 minutes.	53
Figure 29: Transmittance of samples grown at 380°C for 1, 5, and 10 minutes.	54
Figure 30: Transmittance of samples grown at 480°C for 1, 5, and 10 minutes.	55
Figure 31: Transmittance of runs performed for 1 minute at different temperatures.	56
Figure 32: Transmittance of runs performed for 5 minutes at different temperatures.....	56
Figure 33: Transmittance of runs performed for 10 minutes at different temperatures.....	57
Figure 34: Raman spectrum of plain glass substrate.	58
Figure 35: Raman spectra of graphene provided by Army Research Laboratories. Used with permission from Asmaa Elkadi.....	59
Figure 36: Raman spectra of runs performed at 280°C for 1 minute, 5 minutes, and 10 minutes as compared to blank glass.....	60
Figure 37: Raman spectra of runs performed at 380°C for 1 minute, 5 minutes, and 10 minutes as compared to blank glass.....	61
Figure 38: Raman spectra of runs performed at 480°C for 1 minute, 5 minutes, and 10 minutes as compared to blank glass.....	62
Figure 39: Raman spectra of runs performed for 1 minute at different temperatures.	63
Figure 40: Raman spectra of runs performed for 5 minutes at different temperatures.....	64
Figure 41: Raman spectra of runs performed for 10 minutes at different temperatures.....	65

Figure 42: SEM imaging of large flake structures in sample 6.	66
Figure 43: SEM imaging of flake-like structures in sample 7.	67
Figure 45: Multiple nanoflakes of varying diameter.	68
Figure 46: Larger nanoflakes showing a crystalline lattice.	69
Figure 44: Image showing “holes” or “blank spaces” in the graphene lattice [47].	70
Figure 47: Graphical representation of “blank space” in the lattice corresponding to TEM imaging.	71
Figure 48: Zoomed-in image of graphene planes showing the “blank space” spacing.	71
Figure 49: EDX analysis of nanoflakes.	72

List of Tables

Table 1: List of main Raman peaks in graphene [11].	8
Table 2: List of student responsibilities in designing and building the UHV-PECVD system. ...	27
Table 3: List of valves controlled by the switchbox.	34
Table 4: Master run list of experiments performed	47

Chapter 1: Introduction

Current technological advancement in the electronics industry stems from the need for reductions in size and price of the materials used while maintaining or increasing device speed. Semiconductors based on silicon are in wide use today because of the physical and electronic properties of silicon and because of the material's high availability paired with its low cost. In the future, new materials will be needed to keep up with speed, cost, and size requirements. For this reason, the carbon-based material graphene is thought to be silicon's replacement.

Graphene, the single atomic layer of graphite, is the focus of much research today mainly because of its unique electrical properties [1]. It is a zero-gap semiconductor whose band gap can be tuned for specific applications. Electrons in graphene are described as being massless Dirac fermions, meaning that the electron effective mass is zero in graphene. Furthermore, graphene exhibits high mobility at room temperature, higher than $15,000 \text{ cm}^2/\text{V}\cdot\text{s}$. This mobility can drastically improve at low temperatures and is expected to reach at least $100,000 \text{ cm}^2/\text{V}\cdot\text{s}$. Ballistic transport, or electron movement with little to no scattering, is also possible with graphene. This property allows the material to have an extremely high conductivity, even at room temperature [2]. These properties make graphene an excellent material for high-speed applications, such as terahertz devices, and nanoscale devices.

The material cost of graphene fabrication can also be fairly low if the chemical vapor deposition method is used. Chemical vapor deposition, or CVD, uses a combination of gases, heat, and possibly plasma to deposit material on a substrate. In the case of graphene, a carbon-carrying gas is introduced to a heated substrate, usually a metal. The CVD method can be applied to a large-scale process for high yield. It is possible to perform deposition at low temperatures using plasma; therefore, this process is being heavily researched. Characterizing graphene is also

fairly simple and inexpensive, as detailed information on the film's structural properties can be extracted from spectroscopic analysis techniques.

Investigation of the growth of graphene using low-temperature plasma-enhanced chemical vapor deposition (PECVD) is therefore the goal of this thesis. A newly constructed ultra-high vacuum PECVD (UHV-PECVD) system is used to explore the parameter space necessary for graphene growth. Characterization of the grown films was completed using Raman spectroscopy, electron beam microscopy, and optical transmittance.

This thesis is divided into several chapters. In Chapter 2: Graphene, the New Silicon, a description of the material graphene is given, along with an introduction to the growth and characterization methods. Then, a thorough literature review on low-temperature, plasma-enhanced graphene growth is provided. In Chapter 3: Experimental Methods, a description of the UHV-PECVD system designed and built is given. An overview of the single-chamber system used for preliminary graphene depositions is also given. Finally, the experimental procedures for the depositions are discussed. In Chapter 4: Results and Discussion, the results of the characterizations performed on the films are shown and discussed. Finally, in Chapter 5: Conclusion and Future Work, the thesis is concluded and the possibilities of future work on the system are discussed.

Chapter 2: Graphene, the New Silicon

2.1: Characteristics of Graphene

The material graphene is, on its lowest level, composed of a single sheet, or monolayer, of carbon atoms bonded in a “chicken wire” lattice. The structure is often referred to as being the two-dimensional form of graphite. Carbon atoms form a hexagonal structure with 1.42Å bond length of the sp^2 hybridized bonds [2]. Graphite is simply many stacked sheets of sp^2 bonded graphene, with 3.35Å interplanar space length. Carbon nanotubes and buckyballs are also structures that can be formed from rolled sheets of graphene, as seen in Figure 1. In Figure 1(a), the buckyball formation is seen. The buckyball structure is composed of 60 carbon atoms arranged in a “soccer ball” formation. In Figure 1(b), a single-walled carbon nanotubes formation is seen. Single-walled nanotubes are composed of rolled sheets of graphene. In Figure 1(c), the graphite structure is shown. Graphene sheets stacked in an ordered fashion form the material graphite. These structures were originally thought to be the only stable forms of graphene due to its instability at room temperature, though current research has led to fabrication of stable graphene.

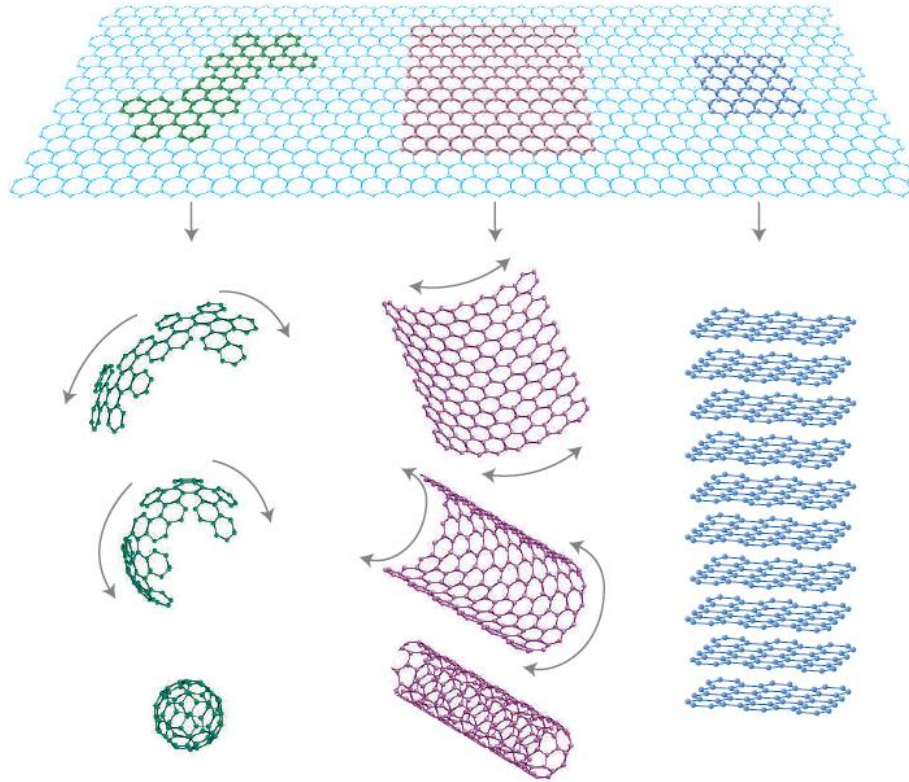


Figure 1: The graphene lattice and other carbon formations [2].

The unique structure of graphene is coupled with equally unique electrical characteristics. Graphene is a semimetal or zero-gap semiconductor. Electronic transport in graphene occurs through massless Dirac fermions, electrons with no rest mass, allowing for a high carrier mobility [3]. Extreme mobilities as high as $100,000 \text{ cm}^2/\text{V}\cdot\text{s}$ have been predicted [2] and recently the room-temperature mobility limit has been pushed to $60,000 \text{ cm}^2/\text{V}\cdot\text{s}$ [4], evidently much higher than the mobility of silicon.

2.2: Chemical Vapor Deposition of Graphene

Though the existence of graphene has been predicted for many years, only in 2004 was it first isolated from bulk graphite. The process of mechanical exfoliation, or “peeling”, has for the first time provided a solution to the problem of single-layer harvesting for characterization purposes [1]. In this process, layers of graphite are repeatedly peeled away (often with tape) until

a single layer of graphene remains. This process, though reliable, is very low-yield and labor intensive, making it unfavorable for practical use. A method of growth allowing for maximum control of graphene properties is therefore needed. The chemical vapor deposition (CVD) method has recently been applied to graphene growth, providing a low-cost and high-yield growth method. Currently there are two main CVD growth processes used in graphene fabrication: high-temperature and low-temperature processes.

Graphene growth at high temperatures of 900°C and above takes place in a two-step diffusion and nucleation process. Hydrocarbon gases used for deposition are thermally broken down at the substrate surface. If metals such as nickel and copper are used as a substrate, carbon atoms physically diffuse into the metal following the solubility limit at the deposition temperature. The large majority of the diffused atoms stay near the surface. When the substrate is cooled and the solubility of carbon in the metal drops, the carbon atoms diffuse back out of the metal and bond, forming graphene. Previously, it has been found that the substrate cooling rate has a distinct effect on this out-diffusion and nucleation process. A “fast” cooling rate of 20°C per second resulted in some carbon reaching the metal surface, though it formed a non-crystalline structure. A “slow” rate of 0.1°C per second resulted in too much diffusion of carbon into the metal, leaving little to no carbon at the surface. The most favorable cooling rate found was a “medium” rate of 10°C per second. This rate was found to allow enough carbon atoms to reach the surface and nucleate, forming graphene [5]. In high-temperature processes, it has been found that copper is favorable to nickel because of its solubility. Though nickel has a higher solubility to carbon than copper, it is not preferred because it leads to too much carbon precipitation and therefore too much growth. A higher amount of carbon enters the nickel and therefore a higher amount exits, leading to a high growth rate. The use of nickel as a substrate

often leads to multilayer graphene (MLG) growth rather than a single layer of graphene. Copper's lower solubility allows for a lower growth rate, leading to a higher chance of graphene growth [6].

For device-oriented processing, such as CMOS applications, it is much more desirable to perform graphene growth at lower temperatures. The growth mechanism at these temperatures is not fueled by the diffusion of carbon into metal because of low solubility and low diffusion coefficient at these temperatures. Lower temperature processes have been developed using plasma to fuel diffusion at the carbon-metal interface.

Plasma-enhanced CVD (PECVD) is the low-temperature growth method studied in this thesis. In this method a noble gas, such as argon, is introduced to the reaction chamber to facilitate in striking a plasma. Electrically excited gas molecules facilitate in breaking down the feedstock, or carbon-carrying gas. The chemically unstable carbon-carrying molecules then deposit on the metal substrate. The hydrogen molecule then breaks off from the gas molecule, leaving carbon to nucleate into a stable formation. Control of the process parameters in PECVD, such as temperature, plasma power, and gas composition are essential to graphene formation.

2.3: Characterization Methods

Identification of graphene can be performed using standard electron microscopy techniques, though this is usually done after performing Raman spectroscopy. For many years, Raman has been the predominant method of not only identifying the presence of graphene but also studying its structure. Besides providing a wealth of information, Raman is also advantageous in that it does not harm the sample and can be performed quickly [7].

2.3.1: Raman Spectroscopy

Raman spectroscopy operates on the principle of inelastic scattering. A laser (usually of visible wavelength) is used to excite a sample. Interactions with the sample will cause the laser light to scatter in one of two ways: elastic or inelastic. This scattered light is then measured. Elastic scattering, when the energy of the incident light is conserved, is the most common. Elastically scattered light will have the same wavelength as incident light, as a photon entering the material will emerge with the same energy with which it entered. Inelastic scattering, when energy is not conserved, results in a very weak signal as this process is less common than elastic scattering. The incident light excites the sample, and the photonic energy is converted to both a lower-energy photon and an optical phonon in the “breathing” lattice. The phonon is produced through a conversion of part or all of the incident energy to kinetic energy, called a Stoke. Scattered light can also combine with a phonon, causing an increase in energy (or Anti-Stoke). These processes strongly depend on the structure and properties of the material. The detected light has different energy than the incident light, called a “shift”. This signal is termed the “Raman” signal, and the detected wavelength (which is then converted to wavenumbers, cm^{-1}) is called the Raman shift. The wavelengths and intensities of the Raman signals resulting from excited graphene can be used to identify and characterize the material [8].

The structure [9] and Raman spectrum of graphite [10] have been studied for many decades. Though graphene is a single layer of graphite, the two materials have similar Raman spectra. Several main peaks are common to both materials (shown in): the D peak at 1360 cm^{-1} , the G peak around 1580 cm^{-1} , and the 2D peak at 2700 cm^{-1} [11]. Additional peaks such as the G' peak (1620 cm^{-1}) and second-order peaks can also be seen. The D peak, or “disorder” peak, is due to phonons produced from scattering at the defect sites in the lattice. It increases with the amount of disorder in the sample. Small crystal size, considered a defect, contributes to this peak

in graphite [10]. In graphene, small grain size causes the D peak to appear. Sampling the Raman spectra at graphene edges can also show a D peak even if the graphene is highly uniform and defect-free [12].

Raman Shift (cm^{-1})	Peak Description
1360	D
1580	G
2700	2D

Table 1: List of main Raman peaks in graphene [11].

In graphene, the G peak and the 2D peak are most commonly studied. The G peak is due to phonon modes of the sp^2 graphene bonds excited by the laser. As the number of graphene layers increases, the intensity of the G peak increases, as more carbon atoms and bonds exist to produce the Raman signal. The 2D peak is essentially a second-order D peak. It originates from a two-phonon double resonance process in the material. In graphite, a wide 2D peak is seen, while graphene exhibits a sharp peak. Using the ratio of the 2D to G peaks, the number of layers of graphene can be estimated. Multiple layers of graphene exhibit a large G peak and small 2D peak, while single layers of graphene exhibit the opposite [13]. This is shown in Figure 2.

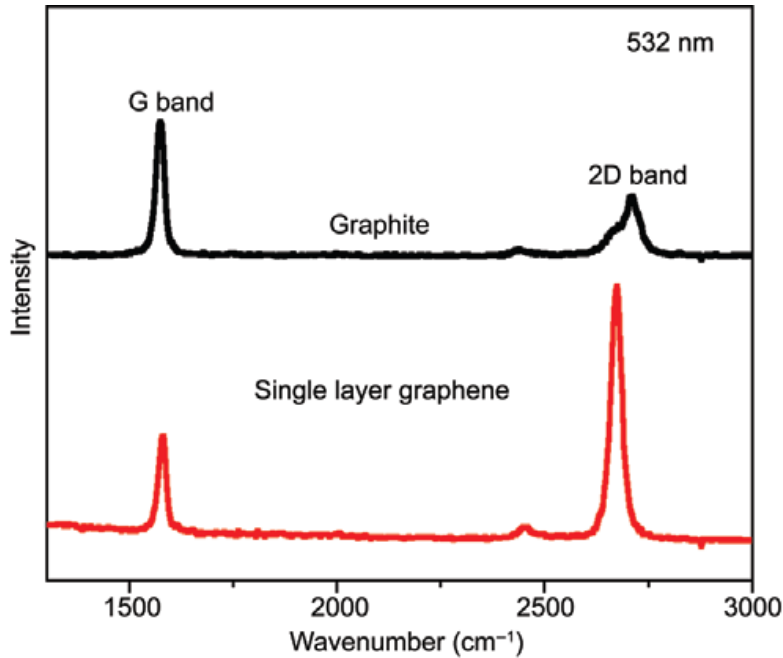


Figure 2: Comparison of Raman signal for bulk graphite and graphene [13].

2.3.2: Electron Microscopy

To visualize graphene, two types of electron microscopy are normally performed: scanning electron microscopy (SEM) and transmission electron microscopy (TEM). SEM imaging normally shows the surface morphology of the deposited film. The thickness and size of graphene formations can be seen this way. A diagram of a simple scanning electron microscope is shown in Figure 3. The mechanism of electron imaging requires an electron gun which produces an electron beam. This beam is focused with magnetic lenses onto a sample, which is normally located in a vacuum chamber. One or more electron detectors are used to detect electrons scattered by the sample. The detected electrons are used to form an image of the sample. Scanning electron microscopy is capable of distinguishing features at sub-nanometer dimensions [14].

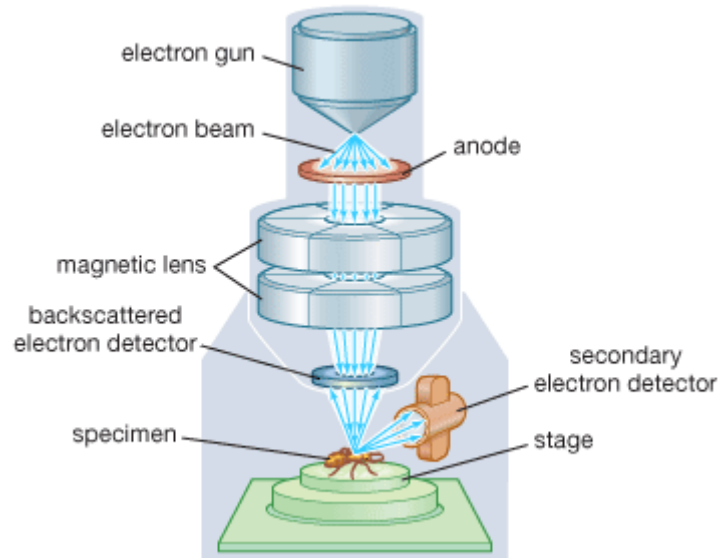


Figure 3: Diagram of scanning electron microscopy imaging mechanism [15].

Transmission electron microscopy imaging is used to investigate the graphene structure. Many types of defects, such as folds, and again the size of the graphene can be seen this way. The number of graphene layers can also be quickly determined using TEM. The mechanism of TEM operation is similar to that of SEM in that it uses an electron gun and magnetic lenses; however, the resolution of TEM can be pushed even higher than that of SEM. This is accomplished through several mechanisms. TEM grids, which are extremely small supporting grids, are used to hold the material. Material observed with TEM must be very thin so that the electron beam can travel through it. The high-voltage electron beam is focused on the sample using the condenser lens. After the beam penetrates and exits the sample, the image is focused using the objective lens. Other lenses, such as the intermediate lens, serve to correct aberration and other imaging problems. The projector lens then magnifies the image so that it can be detected on the fluorescent screen. TEM imaging is currently capable of resolutions as small as 70 picometers [16].

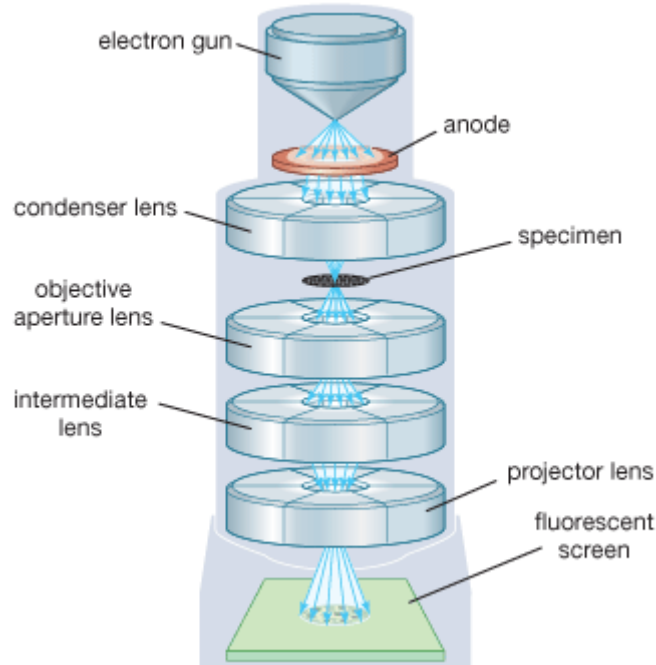


Figure 4: Diagram of transmission electron microscopy imaging mechanism [17].

2.3.3: Optical Transmittance

One additional measurement performed on graphene is optical transmittance, which has been found to indicate the number of graphene layers present. Using white light, it has been determined that each layer of graphene absorbs about 2.3% of incident light. Optical transmittance therefore provides a fast and non-destructive method of determining graphene thickness [18].

2.4: Summary of Graphene Literature Survey

2.4.1: First Isolation of Graphene

It was only recently that graphene has been isolated from bulk graphite. In 2004, K.S. Novoselov, A.K. Geim, and their team at the University of Manchester performed the first known isolation of few-layer graphene (FLG) through the process of mechanical exfoliation. Repeated peeling of highly-ordered pyrolytic graphite (HOPG) produced single, double, and

triple layers of graphene [1]. In 2005, this group investigated electron transport in graphene. It was found that electrons operate as massless Dirac fermions, giving graphene a very unique class of electrical characteristics [3]. In 2008, a method for determining the number of graphene layers through simple optical characterization was developed. For each layer of graphene present, approximately 2.3% of incident white light is absorbed [18].

2.4.2: Thermally-Induced Growth

After the first isolation of graphene, focus shifted to graphene fabrication. In 2008, Qingkai Yu and other researchers at the University of Houston first proposed the growth mechanism of graphene at high temperatures. A three-step process was demonstrated using nickel foils as the substrate. First, the nickel was placed into a heated chamber at 1000°C. Second, methane gas was introduced to the substrate. Lastly, after 20 minutes exposure to methane, the gas was turned off and the samples were placed into a controlled cooling environment. The effect of the cooling rate was studied at three different rates: 0.1°C/s, 10°C/s, and 20°C/s. Raman spectroscopy was performed on each of the samples and the results were used to characterize the effects of the cooling rate. A slow rate of 0.1°C/s was found to correlate with no peaks in the Raman spectrum. This indicates no carbon at the surface of the metal. A medium rate of 10°C/s showed both the G and 2D peaks, with the intensity ratio of the 2D to the G being more than one. Therefore, a small number of layers of graphene with good crystallinity have formed on the sample. A fast cooling rate of 20°C/s showed D, G, and 2D peaks. The presence of the D peak and the intensity ratio of the 2D to G peak being less than one indicated that carbon atoms had reached the surface of the metal, but did not form a highly crystalline material. These results indicate that a slow cooling rate allows carbon atoms too much time to diffuse into the nickel, while a fast cooling rate does not allow the film to form into a crystalline

structure. This process is illustrated in Figure 5. Additional findings included that hydrogen has the ability to remove dangling bonds from the graphene layer and defects in the films as well as to protect the films from impurities (for example, sulfur and phosphorous) [5].

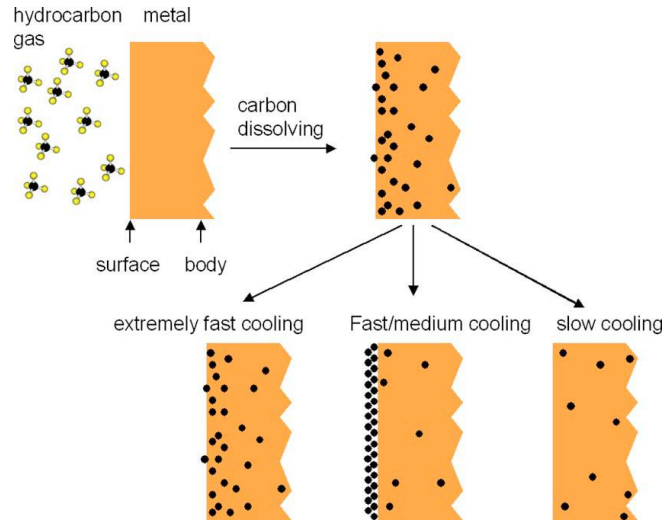


Figure 5: Growth mechanism of thermal CVD [5].

The cooling rate in high-temperature CVD processes was also investigated by Yasumitsu Miyata et al. at Nagoya University. Graphene was synthesized on nickel foils at 900°C inside a quartz tube. Ethanol was used as the carbon source. The ethanol was bubbled with Argon into the quartz tube for five minutes. After this, the tube was cooled from 900°C to 560°C at the rate of 30°C/s, termed “flash cooling”. Raman spectroscopy was used to characterize the films after they were transferred to an oxidized silicon wafer. A small D peak, large G peak, and larger 2D peak were seen using a 633nm laser. No graphene was detected on samples cooled naturally (at 0.3°C/s). Also, no graphene was seen on samples that were naturally cooled to 850°C and then flash cooled, which indicated diffusion of the carbon atoms into the substrate. A substrate with lower carbon solubility, such as copper, would allow for less diffusion and therefore less carbon layers to form on the surface [19].

Synthesis of graphene through heat-based processes poses an efficiency challenge. High deposition temperatures that produce low output coupled with structurally imperfect films do not make for efficient synthesis techniques. A method proposed by Xuesong Li et al. at the University of Texas at Austin has provided a solution to this. Graphene films of one layer were grown on 300 mm copper films on silicon. The copper films were annealed prior to growth, which was performed at 1000°C using methane and hydrogen. Growth times varied from less than 10 minutes to 60 minutes. Raman spectroscopy was performed on the films for characterization. Single-layer areas showed a G peak and a 2D peak, with the 2D peak being approximately twice as intense as the G peak. Double-layer areas showed the G and 2D peaks, with the 2D peak only slightly more intense than the G peak. Areas with three layers showed a very intense G peak, a weak 2D peak, and a weak D peak, indicating an area of disorder in the films. Films grown for much less than 10 minutes showed sporadic nucleation at different locations on the foil. A growth time of 60 minutes showed results comparable to a 10 minute growth, indicating that the growth mechanism is self-limiting. This result also indicates that the growth mechanism may be fueled by surface interactions rather than a diffusion process [20].

Large graphene films of 1cm² area were produced by Seung Jin Chae et al. at the Samsung Advanced Institute of Technology. In this study, the effects of the substrate deposition temperature, the hydrocarbon gas mixture, and the deposition time were investigated. Temperatures studied ranged from 700°C to 1000°C with constant growth time and gas mixture for this set of experiments. Acetylene gas (C₂H₂) was used as the carbon source. It was mixed with hydrogen at different ratios: 2 sccm C₂H₂:45 sccm H₂, 3:45, 5:45, and 10:45. For this set of experiments the temperature was held at 1000°C and the growth time was 5 minutes. To evaluate the quality of the graphene films at these different parameters, Raman spectroscopy was

performed with a 633 nm laser. At the 700°C growth, a D peak is seen, indicating defects in the graphene. At higher temperatures, this peak is not seen. In all samples, a G and 2D band is seen, with the 2D band always being more intense than the G band. This shows that the graphene has formed less than 5 layers. For the 1000°C growth with varying gas mixtures, no D peak is seen at all. The G and 2D peaks are very easily seen, however. A downshift in the position of the 2D peak is seen with decreasing carrier gas concentration. The intensity of the 2D peak as compared to the G peak was highest at a ratio of 2:45. Interestingly, no graphene was formed in the absence of hydrogen. Therefore, the lowest number of layers was achieved with the 2:45 ratio, suggesting that hydrogen has an etching effect on the graphene to keep it from forming multiple layers. Lastly, the effects of growth time on the substrate were studied. Growth times of 5, 10, and 15 minutes were studied while the temperature was kept at 1000°C and the gas mixture at 2:45. To evaluate these effects, Raman spectroscopy using a 514 nm laser was performed. Increased growth times produced an increasing upshift and decreasing intensity of the 2D peak as compared to the G peak. This indicates that more layers are formed with longer growth times. The results of this paper indicate that few-layer, highly-crystalline materials form when there is a large amount of hydrogen gas as compared to carrier gas, when the temperature is high, and when the growth time is short [21].

2.4.3: Plasma-Enhanced Growth

Low-temperature growth, specifically growth at and below 700°C, has been the more recent focus of graphene fabrication methods. The possibilities of implementing low-temperature growth for building and enhancing devices are endless. In 2004, one of the first steps toward low-temperature growth was taken by Jianjun Wang et al. at the College of William and Mary. Graphene sheets were fabricated at as low as 600°C on many substrates including silicon, SiO₂,

and copper. An inductively-coupled 900 W power plasma generated by a 13.56 MHz RF signal was used for deposition. Resistive heating was used to heat the substrates. Methane, the carbon source, was mixed with hydrogen gas for a total gas flow of 10 sccm. The amount of methane was varied from 5% to 100% of total flow. The pressure inside the quartz tube reactor was kept at approximately 90 mTorr. Results of the process were characterized by scanning electron microscopy and Raman spectroscopy. It was found that temperatures less than 600°C did not produce any graphene sheets. Furthermore, the highest growth rate was found at 100% methane concentration and 825°C. However, the quality of graphene sheets grown with these parameters is not as good as those grown at 10% methane concentration (with temperature held at 680°C and a growth time of 20 minutes) and 630°C (with methane concentration held at 40% and a growth time of 20 minutes). This is evidenced in the Raman spectrum of these samples. Studies of films grown with 10% concentration show a slight D peak, large G peak, and large 2D peak. This indicates a low number of layers in the graphene flakes and some defects. In contrast, films grown at 100% concentration show a large D peak, smaller G peak with D' shoulder, and smaller 2D peak. This would indicate that the number of defects in the flakes is higher at higher concentrations. Samples grown at higher temperatures show similar results. The intensity of the D peak and the D' shoulder relative to the G and 2D peaks increases with temperature. This also indicates sheets with more defects [22].

Wang's research was furthered in 2007 by Mingyao Zhu of the same research group. In this study, the effects of RF power and chamber pressure on the films were investigated. The RF power was varied from 400 W to 1200 W, and chamber pressure was varied from 20 to 400 mTorr. Raman spectroscopy and SEM confirmed that the uniformity and quality of the nanosheets increases with increasing RF power and increasing pressure. It was found that lower

pressures facilitated faster growth, though more defects were present in the material. Furthermore, higher RF power increases the amount of hydrogen etching on the graphene, allowing for more ordered films [23].

Mingyao Zhu also investigated growth of graphene sheets over carbon nanotubes using an inductive plasma. In experiments similar to before, the plasma power varied from 400 to 1200 W. The substrate used was nickel-patterned silicon, which was cleaned with NH_3 etching prior to deposition. The gases used for deposition were CH_4 , H_2 , and C_2H_2 . The deposition was performed for 20 minutes at a temperature of 680°C . A number of characterization techniques were used with similar results as previously found. However, it was seen that graphene sheets would grow on top of nanotubes which were first deposited. The nanotubes were grown with 20% CH_4 in H_2 using a capacitive plasma for a duration of 5 minutes. After this, the graphene sheets were grown, showing that a single system can be used for both nanotubes and graphene deposition [24].

Microwave plasma sources have also been used to fabricate graphene. Alexander Malesevic et al. used a high-powered 2.45 GHz cylindrical microwave resonator as both the plasma and heat source. The depositions were performed at 700°C at a pressure of 40 Torr on many substrates including quartz, silicon, and nickel. Methane and hydrogen, at flow rates of 22 and 178 sccm respectively, were used to deposit for times ranging from 1 second to 50 minutes. The RF power used during deposition was 2 kW. No deposition was possible at temperatures below 700°C . SEM, TEM, Raman spectroscopy and many other methods were used to characterize the results. SEM images showed that the graphene was formed in sheets which were aligned vertically to the substrate. TEM confirmed an average sheet thickness of 4 to 6 layers. Furthermore, Raman spectroscopy showed the usual G and 2D bands, along with a less intense D

band and a D' shoulder. This indicates a small degree of disorder in the flakes. Analysis of samples grown for different durations showed a three-step growth process. First, a layer of graphite containing cracks and folds forms on the surface of the substrate. Second, graphene sheets grow perpendicular to these defects. Third, the sheets grow taller and wider. It was also found that higher ratios of hydrogen to methane caused a decrease in the size of the flakes [25].

The temperature barrier was pushed lower in 2009 by G.D. Yuan et al. at the City University of Hong Kong. A commercial reactor was used to perform depositions for 20 minutes at a low vacuum of 30 Torr. Hydrogen and methane at flow rates of 180 sccm and 20 sccm, respectively, were used for deposition. A microwave plasma at 1.2kW power was used. Though the temperature on the substrate holder was 800°C, graphene flake-like growth was seen on the wall of the reactor chamber, which was at a temperature of 500°C. Characterization was performed with SEM, TEM, atomic force microscopy, and Raman spectroscopy. SEM images showed large, uniform sheets approximately 10 μm x 20 μm in size. TEM indicated that the sheets are smooth and uniform. Raman spectroscopy indicated slight disorder with a D peak at 1329 cm⁻¹, but a strong G peak at 1580 cm⁻¹ and strong 2D peak at 2653 cm⁻¹ show that the graphene is single-layer [26].

Capacitively coupled plasma has also been researched in graphene growth. In 2004, M. Hiramatsu et al. studied the effects of capacitive plasma on graphene growth. The feedstock gases C₂F₆, CH₄, and CF₄ at a flow rate of 15 sccm were used along with hydrogen at 30 sccm flow. The chamber pressure was 100 mTorr and the capacitive plasma power was 100 W. Substrate heating was set to 500°C and the growth time was varied from 15 minutes to 8 hours. The substrates used were (100) and (111) silicon, fused silica, and sapphire. The growth process produced vertically aligned nanosheets that were characterized by SEM and Raman

spectroscopy. The structure of the sheets was seen to be similar across all substrates. The Raman spectrum shows both G and D peaks, indicating a carbon formation with defects [27].

The use of remote plasma has also been used to perform low-temperature depositions. In 2010, Nandamuri et al. achieved graphene deposition using remote plasma of 250 W power at temperatures ranging from 650°C to 700°C. The pressure was held at 90 mTorr with 2.5 sccm CH₄ and 8 sccm H₂ gas flow. The deposition was performed for 1 minute on Ni/SiO₂/Si, with layer thicknesses of 200 to 300 nm Ni (deposited with e-beam evaporation) and 100 nm SiO₂. E-beam evaporation of 200 to 300 nm of Ni was also performed on Ni foil of 1 micron thickness and (111) oriented nickel. The nickel films were annealed at 1000°C to increase grain size. The samples were analyzed using Raman spectroscopy, optical transmittance, and TEM. Raman spectroscopy using a 532 nm laser showed a G peak at 1580 cm⁻¹ and a 2D peak at 2690 cm⁻¹. Optical transmittance on films transferred to glass microscope slides showed that about 7 layers of graphene were present. TEM imaging confirmed the hexagonal structure of the graphene. Furthermore, a back-gated transistor was used to measure the graphene mobility, which was found to be 3000 cm²/V•s. It was found that the size of graphene films highly correlated to the grain size of the substrate, which would indicate epitaxial growth. The films were grown with only methane flowing, but Raman analysis showed defects in the graphene. Runs without plasma were performed and no growth was seen [28].

Extreme low-temperature synthesis was performed on polycrystalline nickel foil by Kim et al. in 2011. Depositions were performed from 450°C to 750°C in a 2.45 GHz microwave plasma CVD reactor. The plasma power was 1400 W and the chamber pressure was kept at 20 Torr. Various hydrogen to methane flow rate ratios were used for deposition: 80:1, 40:1, 20:1, and 10:1 sccm. The cooling rate of the substrate was controlled and kept at 3°C per second. After

deposition, the films were transferred to SiO₂ on Si and polyethylene terephthalate (PET) for characterization. Raman spectroscopy and TEM characterizations were performed on the films. It was seen that films grown at a gas ratio of 80:1 at 750°C gave a strong 2D peak and slightly less strong G peak, though the D peak was very small. As the ratio decreased, the G and 2D peaks decreased in intensity and the D peak increased. This would indicate that a mixture of 80:1 is optimal for high quality, large-scale graphene, a result confirmed by TEM imaging. Raman spectroscopy performed on samples of varying temperature with the 80:1 ratio show that higher temperatures also lessen the D peak and increase the G and 2D intensities. Films grown at 450°C had a D peak of approximately the same intensity as the G peak, which was about half the intensity of the 2D peak. This result indicates that few layer graphene films were grown at lower temperatures, but there were a large number of defects [29].

Surface wave plasma has also been investigated as a method of graphene deposition. In 2011, J. Kim et al. were able to perform large-area synthesis of graphene at temperatures lower than 400°C. A surface-wave plasma CVD system was used at high power (3 to 4.5 kW) to deposit films for 30 seconds to 3 minutes on copper and aluminum foil. A mixture of methane, argon, and hydrogen was used in the ratio of 30 CH₄: 20 Ar: 10 H₂ sccm at a pressure of 38 mTorr. Before the deposition process was started, Ar and H₂ plasmas were used to clean the substrate for 20 minutes. After deposition, the films were characterized by Raman spectroscopy, and then transferred to other substrates for optical transmittance and sheet resistance studies. Using a wavelength of 638 nm, the D (1326 cm⁻¹), G (1578 cm⁻¹), 2D (2657 cm⁻¹), and D' (1612 cm⁻¹) shoulder peaks were seen. The ratio of the 2D to G peaks was seen to be 3.4, and the presence of a D peak indicated a single graphene layer that is broken into micrometer-sized flakes. Optical transmittance showed an average of 81% transmission in the range of 400 to 800

nm. The sheet resistance ranged from 2.2 to 45 k Ω /square. The resulting graphene was used to fabricate a capacitive touch panel [30].

Recently, graphene fabrication was performed by microwave plasma chemical vapor deposition at 400°C. Tamada et al., of the same group as Y. Kim, used a 20 kW 2.5 GHz surface wave plasma to generate graphene films roll-to-roll on a copper substrate. The temperature was monitored directly on the copper substrate and kept at 400°C throughout the process. The pressure was kept at 225 mTorr. Gases used in deposition were methane, hydrogen, and argon, at flow rates of 30, 50, and 20 sccm. After synthesis the films were transferred to PET. Multiple characterizations were performed on the films including Raman spectroscopy, optical transmittance, and TEM. Raman spectra show the D, G, and 2D peaks, with the intensity of the D peak being comparable to the G and 2D peaks. This indicates a graphene layer with defects which most likely stem from the transfer process. The optical transmittance averaged 95.2% from 400 to 800 nm. TEM imaging showed a graphene structure with 3 and 4 layers [31].

The use of alloys as catalysts has also been recently investigated. In 2011, E.S. Kim et al. fabricated few-layer graphene using a palladium-cobalt alloy. The use of this alloy allowed for deposition at the low temperature of 400°C. Higher temperatures, 500 and 600°C, were also studied. The plasma power used was 250 W and the gas mixture was 5:45 sccm C₂H₄:H₂. The growth was performed for 5 minutes. Nickel was also investigated in this study. After transferring the graphene to a 300 nm SiO₂ on Si and glass substrates, several methods of characterization were performed including Raman spectroscopy, high-resolution TEM, and optical transmittance. The PdCo alloy produced a Raman signal containing the D, G, and 2D peaks. Samples formed at the lowest temperature gave a lesser D to G peak ratio than samples formed at higher temperatures. This is due to the alloy's ability to remove the hydrogen present

in the gas molecule. For the nickel substrate, no Raman signal was detected at 400°C. There were signals from the 500 and 600°C runs that showed the D, G, and 2D peaks. However, with decreasing temperature the ratio of the D to G peak increased, opposite of what was found for the PdCo alloy. TEM imaging confirmed the presence of graphene films formed on the PdCo alloy at 400°C. Furthermore, optical transmittance showed a total of 88% transmittance, indicating that about 5 graphene layers were present [32].

High quality graphene has been fabricated using a combination of PECVD and high temperatures. Recently, Lam Van Nang et al. used an inductively coupled plasma varied up to 600 W to deposit graphene on copper foil at 950°C. The pressure was kept at 1 Torr and the gas flow rates were 1 sccm CH₄: 10 sccm H₂: 90 sccm Ar. Deposition was performed for times ranging from 5 seconds to 60 minutes. The results were characterized using Raman spectroscopy, high-resolution TEM, optical transmission spectroscopy, and sheet resistance. Raman spectroscopy using a 514 nm laser showed D, G, 2D, and D' peaks. The D peak was seen to decrease and the 2D peak to increase with increasing growth time, suggesting a better graphene structure with fewer layers. A five-second growth produced the most intense D peak seen. HRTEM imaging was used to confirm the structure of the graphene, and it was seen that a 5 minute growth time gave optimal results with mostly single and bi-layer graphene. Optical transmission averaged 96.6% over the visible range, which indicates between 1 and 2 layers of graphene. Lastly, the sheet resistance was found to vary depending on the growth time. A five-second growth produced 5.2 kΩ/square, while a 5-minute growth gave 1.95 kΩ/square. This indicates that the sheet resistance is related to the amount of structural defects, with fewer defects giving a more conductive sample. It was seen that at higher temperatures, hydrogen etching does

not remove the first carbon layer because the rate of carbon chemical adsorption overcomes the rate of hydrogen etching [33].

Fast graphene growth was recently investigated by Kumar et al. using a commercial microwave plasma CVD system. The growth time was varied from 30 seconds to 2 minutes with a 400 W plasma and 10 Torr pressure. Methane at a 10% concentration in hydrogen was used as the carrier gas, with a total flow of 55 sccm. Copper foil was used as the substrate. The substrate was not independently heated, but the temperature due to the plasma alone was observed to be approximately 700°C. The total growth process took less than 5 minutes total. Many types of characterization were performed, including Raman spectroscopy. A 514 nm laser was used for Raman, which showed a D peak for all growth times. The D peak was seen to decrease in intensity with increasing growth time [34].

Graphene fabrication has also been performed without the use of substrates. Albert Dato et al. and the Applied Science and Technology Graduate Group at the University of California, Berkeley, demonstrated a method of fabrication using microwave plasma CVD that does not require a substrate. An argon plasma using a 2.45 GHz signal at 250 W power was struck inside a quartz tube at less than 150 Torr, to which ethanol was then introduced. Filters located downstream from the plasma were used to collect the films. TEM and Raman spectroscopy were used to analyze the films. TEM images showed single-layer sheets, but they were largely non-uniform, containing multiple folds. Raman spectroscopy, performed with a 40 mW laser, showed 2D, G, and D peaks. A D' shoulder on the G peak was also seen at 1620 cm^{-1} . This indicates the presence of a single layer of graphene with defects, which could show folds or even edges if the laser were positioned on an edge [35].

2.5: Outline of Research Goals and Objectives

The goal of this thesis is two-fold. First, a system suitable for performing not only graphene depositions but also many other types of thin film depositions is desired. This was to be accomplished by an interdisciplinary team of graduate students working under supervision of experienced professors and staff. Second, preliminary depositions were to be performed on a similar CVD system to prepare for deposition on the main CVD system being built. In these preliminary depositions, the parameter space for low-temperature graphene growth was to be investigated. The single-chamber CVD system in room 350B of the ENRC was used for these depositions. The as-grown films were characterized using Raman spectroscopy, electron microscopy, and optical transmittance.

Chapter 3: Experimental Methods

3.1: The UHV-PECVD System

The methods for graphene deposition involve very specific capabilities. High-purity atmospheres, plasma enhancement, and substrate heating are only a few of the necessary elements. For this reason, the Ultra-High Vacuum Plasma-Enhanced Chemical Vapor Deposition (UHV-PECVD) system in Room 350C of the Engineering Research Center was built.

In 2010, a team of professors, post-docs, students, and staff at the University of Arkansas began designing and building a machine capable of multiple types of thin film and nanoscale depositions. From the start, the team's main concern was safety. Because of the nature of the gases used in the semiconductor industry, each aspect of the system was reviewed carefully before implementation.

With careful guidance by Dr. Hameed Naseem, Dr. Fisher Yu, Dr. Husam Abu-Safe, and Dr. Zafar Waqar, a team of graduate students consisting of Benjamin Conley, Shannen Adcock, Aboozar Mosleh, and Bryant Hankton carefully chose the main parts of the system. Each student was in charge of different aspects of the system, as shown in Table 2. Though each student worked separately on his or her responsibilities, each week the team of students met to discuss progress on their respective parts. Collaboration was key for ensuring all system components would work together to produce a truly cutting-edge system.

Graduate Student	System Responsibilities
Benjamin Conley	1. Gas delivery system: Process gas tubing, pneumatic valves, and mass flow controllers 2. Vacuum pumps and gauges: Turbo and mechanical pumps, pressure gauges, and chiller

	<p>3. System safety features: Documentation, tubing enhancements, and structural enhancements</p> <p>4. System construction</p>
Shannen Adcock	<p>1. RF source and matching network</p> <p>2. Gas abatement system</p> <p>3. Pneumatic valve control system: Manual control and computer control</p> <p>4. Gases: Gas ordering and regulators</p> <p>5. System safety features: Documentation, gas alarm system, exhaust and exhaust alarm systems, electrical and structural enhancements</p> <p>6. System construction</p>
Aboozar Mosleh	<p>1. Plasma arm: plasma electrode design and construction</p> <p>2. Gas delivery system: process gas tubing, mass flow controller recalibration and ordering</p> <p>3. Vacuum pumps and gauges: pressure gauges and chiller ordering</p> <p>4. Substrate holder ordering</p> <p>5. System safety features: Documentation, exhaust and secondary containment systems</p> <p>6. System construction</p>
Bryant Hankton	<p>1. Substrate holder: Specification of holder design to system needs, transfer arm fork, sample rotation program, sample transfer process</p> <p>2. Sniffers</p> <p>3. System safety features: Documentation, overheat warning and</p>

	shutoff system for mechanical pump
	4. System construction

Table 2: List of student responsibilities in designing and building the UHV-PECVD system.

Beginning in late 2010, finalization of the system components was started and the next step, ordering the components, began. Most large system components such as the gas abatement system and substrate holder were ordered in early 2011. The maximum lead time on select components was approximately 6 months, therefore system construction began in late spring of 2011. The main construction period extended until the fall of 2011, however small system enhancements are still currently taking place. During the construction period, constant guidance from Dr. Hameed Naseem was provided to the students. Staff members from the High Density Electronics Center, notably Mike Steger and Tom Cannon, and from the Engineering Research Center, notably Mike Brosius, were also consulted.

Due to the complexity and the special capabilities of the UHV-PECVD system, documentation on system design, construction, and use was essential. Many documents for the system were developed by the students building the system. A construction manual detailing the procedures and safety measures taken while building the system was authored by the team. Also, a technical manual with information on the subsystems of the UHV-PECVD system was written. Additional documents, such as the gas cylinder change protocol, a guide to reporting emergencies, a maintenance schedule, and guides for using the system were written. These documents will serve multiple purposes for the research group. New students will be able to read these documents and easily understand how the system components work together after being trained. When maintenance to the system is needed, these documents will serve as a guide.

3.1.1: Design of the UHV-PECVD System

The UHV-PECVD System was designed and built to perform ultra-high vacuum thin film depositions. It is composed of two main vacuum chambers, the load/lock and process chamber. Wafers are loaded into the load/lock, transferred to the process chamber for deposition, and then transferred back to the load/lock to be unloaded. A schematic of the system is shown in Figure 6.

Ultra-high vacuum processes are needed to maintain device purity. Pumping a chamber down to UHV levels ensures that a low number of gas molecules and impurities are present before the deposition is started. Plasma enhancement is necessary for performing depositions at low temperatures. In the case of graphene, plasma helps to break down the hydrocarbon gas and fuels carbon deposition on the substrate surface. Low-level sample heating is also used in most graphene depositions to encourage the deposition process. These necessary processes were implemented as the base of what the UHV-PECVD system can accomplish.

High vacuum processes are possible through a series of mechanical and turbomolecular pumps mounted on both chambers. In the process chamber, a cryogenic pump is used to remove water vapor from the ambient air. The system is equipped for many gases including silane, methane, germane, stannane, hydrogen, phosphine, boron trichloride, diborane, argon, and nitrogen. A substrate holder with rotation and heating capability is used for substrate processing. Plasma enhancement has been implemented through the use of a 13.56 MHz radio frequency source which is biased across a plasma arm and the substrate holder.

Chamber 1, the load-lock, is equipped with two pumps: a mechanical pump and a turbomolecular pump. The mechanical pump is an Edwards XDS10 dry scroll pump, seen in Figure 6(a). Scroll pumps operate using two scrolls: a fixed scroll and an orbiting scroll. The orbiting scroll compresses the gas that enters the pump and pushes it toward the center of the fixed scroll. It is then exhausted from the pump [36]. The turbomolecular, or “turbo” pump, is a

Pfeiffer TMU400M, seen in Figure 6(e). Turbo pumps operate in a fashion similar to a fan. A magnetically levitated fan rotor equipped with steel blades is rotated at around 50,000 RPM. Any molecules that come into contact with the rotor blades are pushed toward the exhaust port at very high speeds [37]. Magnetic levitation is extremely beneficial to the pump because it allows for frictionless rotation. The turbo pump is at all times backed by the mechanical pump. The combination of these two pumps allows for a high vacuum level to be reached in the load-lock chamber.

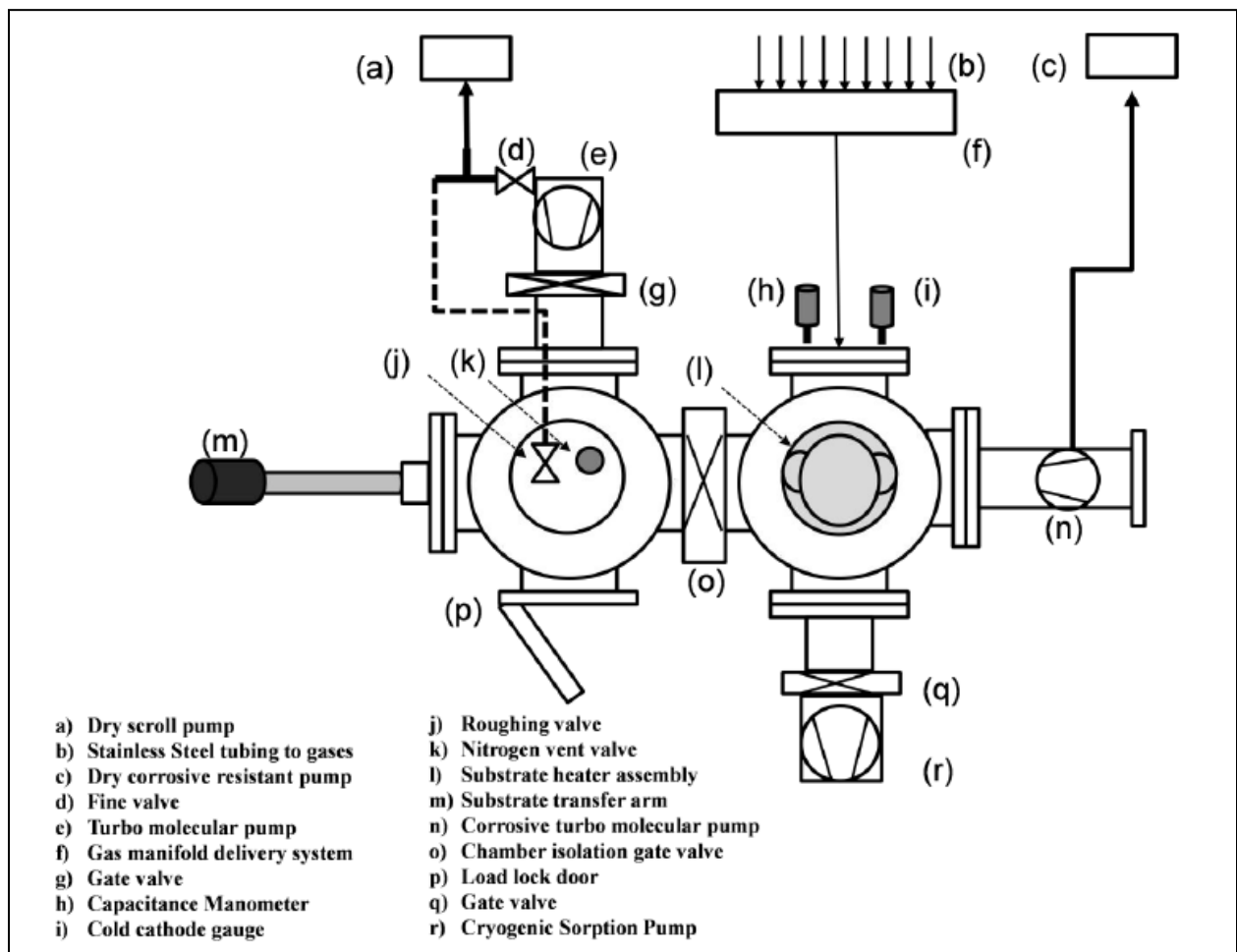


Figure 6: Diagram of the UHV-PECVD System [38].

Chamber 2, the process chamber, also has both a mechanical and a turbo pump. Due to the exposure of these pumps to process gases, they must be equipped for operating in a corrosive

environment. The mechanical pump, an Edwards QDP40, is a dry rotary pump, as seen in Figure 6(c). It is equipped with four stages of positive displacement rotary pumps [39]. The turbo pump, an Edwards STP451, is similar to the Pfeiffer TMU400M in method of operation. It can be seen in Figure 6(n). This pump has magnetically levitated rotor blades allowing for high-speed rotation [40]. Both the mechanical pump and the turbo pump are equipped with materials that will not interact with the process gases. All machine parts and exhaust lines are made of corrosion-resistant material. The process chamber also employs a non-corrosive pump, the cryogenic or “cryo” pump, for removal of water vapor when the chamber is not in use. It can be seen in Figure 6(r). The Sumitomo CP-8 cryo pump works by trapping gases in the chamber on a cryogenic refrigerator (cold head) that is cooled by liquid helium injection. When water vapor, nitrogen, oxygen, or argon reaches the cold head, it is frozen in place. Furthermore, a charcoal filter is used for capturing gases that do not freeze at the cold head temperature, such as neon, hydrogen, and helium [41].

To monitor the vacuum in the system, several different types of gauges are used. The load-lock chamber is equipped with a Pfeiffer FullRange Gauge, which is a combination of two types of gauges: Pirani and inverted magnetron cold cathode [42]. Pirani gauges work by taking advantage of the resistance change across a heated filament exposed to vacuum. When gas molecules hit the filament, heat is removed from it, causing the filament to cool. This changes the resistance and therefore a change in the applied current is needed to maintain the filament at the same temperature. This can be correlated to the vacuum level in the chamber. Pirani gauge measurements range from atmospheric pressure down to 10^{-4} Torr [43]. The inverted magnetron cold cathode gauge is a type of ionization gauge. A high voltage is applied across an anode and cathode, which ionizes the gas present. The current is monitored on a collector and can be

correlated to the vacuum level. This type of gauge can measure pressure from 10^{-4} to 10^{-11} Torr [44]. Measuring the vacuum in the process chamber requires methods suitable for corrosive environments. A cold cathode gauge is therefore also employed on chamber 2, shown in Figure 6(i). Another type of gauge, the capacitance manometer gauge, is used to monitor pressure from atmosphere to 10^{-4} Torr in this corrosive environment. It is shown in Figure 6(h). The capacitance manometer, or Baratron, measures vacuum by monitoring the capacitance between an electrode and a conductive diaphragm exposed to the vacuum chamber. A very high vacuum is applied between the electrode and diaphragm using a chemical getter pump. The diaphragm will move in an amount that can be correlated to the vacuum level of the chamber. The diaphragm is sensitive to vacuum levels much lower than what is maintained between it and the electrode [45].

3.1.2: Design of Control Systems

Control of the UHV-PECVD system is performed through multiple mechanisms. Setting the mass flow controllers, operating the substrate holder, operating the plasma, controlling the pumps, and controlling the vacuum gauges are performed through specialized control systems provided with each instrument. For gas flow control, a system of pneumatic valves has been implemented. The pneumatic valves are the largest part of the control system; control of them is critical to system operation. Many electrical solenoids are used to pneumatically actuate the valves. They are controlled by switching 120VAC on or off, as shown in Figure 7. For this reason, an electrical switchbox was built to turn the solenoids off and on, shown in Figure 8. The switchbox allows the user full manual control over 30 of the main valves in the system. A map of these switches with valve numbers is shown in Figure 9. Additional switchboxes were installed for further sub-systems such as the process exhaust. The switches interrupt the 120 VAC line

connected to the valves. Hence, each valve is always connected to ground, but the user turns them on by flipping the associated switches, allowing 120 VAC to reach the valves and turn them on. Power to the switchbox is connected to an uninterrupted power supply so that the system is protected in the event of power failure. An emergency stop button is connected to the switchbox that, when pressed, closes all valves on the switchbox in the event of an emergency. Valve identification numbers are provided in Table 3.

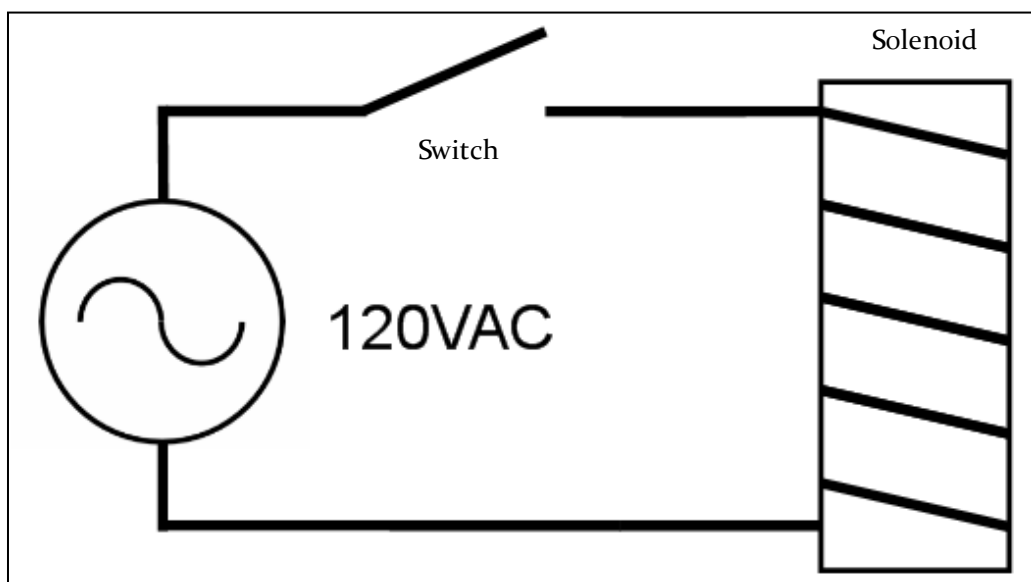


Figure 7: Diagram of solenoid on/off switching mechanism.

The layout of the switchbox was designed with ease of use in mind. Switches related to controlling the path of the process gases were grouped according to gas. For example, stannane and boron trichloride each have entry, chamber entry, and purge valves. For these two gases, each entry type is on the same row. The same applies for diborane, argon, nitrogen trifluoride, phosphine, silane, and germane controls: the entry valves are all on the top row, and the purge valves are on the middle row. Methane and hydrogen do not have separate purge valves, so their entry valves are along the top row. Below these two gases the main entry and purge valves are also listed. All the gas labels are also color-coded for easy identification.



Figure 8: Photograph of main switchbox layout.

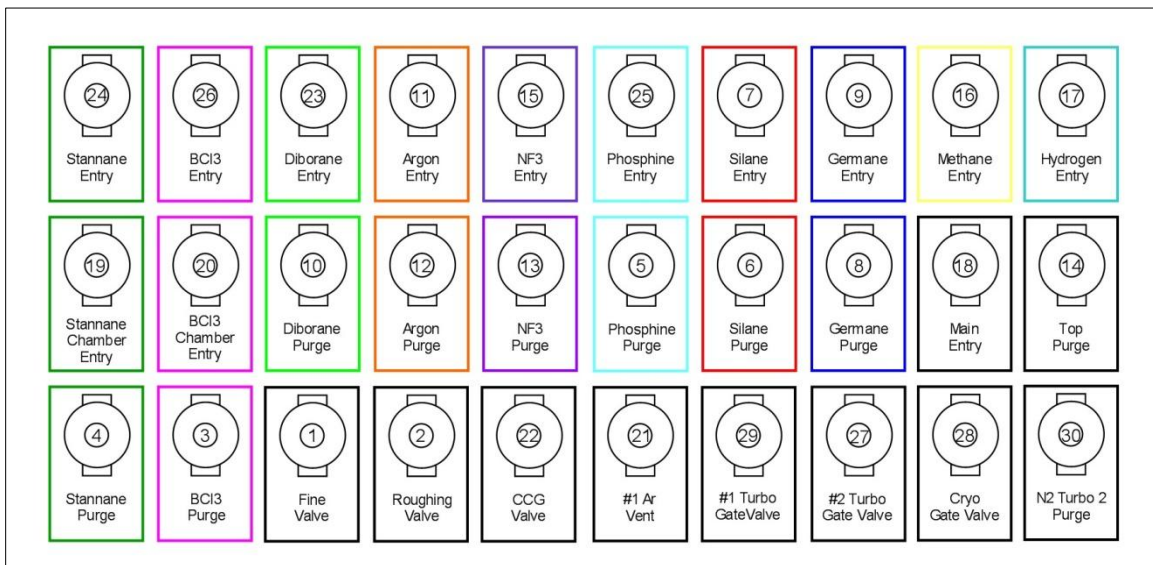


Figure 9: Map of main switchbox layout with valve numbers shown.

Valve controls not directly related to process gas flow are located on the third row. The fine and roughing valves on chamber 1 are grouped together. The turbo pump gate valves and nitrogen purging for the chamber 2 turbo pump are also grouped.

1	Fine Valve	16	Methane Entry
2	Roughing Valve	17	Hydrogen Entry
3	BCl3 Purge	18	Main Entry
4	Stannane Purge	19	Stannane Chamber Entry
5	Phosphine Purge	20	BCl3Chamber Entry
6	Silane Purge	21	#1 Ar Vent
7	Silane Entry	22	CCG Valve
8	Germane Purge	23	Diborane Entry
9	Germane Entry	24	Stannane Entry
10	Diborane Purge	25	Phosphine Entry
11	Argon Entry	26	BCl3 Entry
12	Argon Purge	27	#2 Turbo Gate Valve
13	NF3 Purge	28	Cryo Gate Valve
14	Top Purge	29	#1 Turbo Gate Valve
15	NF3 Entry	30	N2 Turbo 2 Purge

Table 3: List of valves controlled by the switchbox.

Control of the 30 main valves is also possible using a LabVIEW program. To use this, a National Instruments cDAQ-9178, was purchased to interface with the computer. The cDAQ, or compact data acquisition system, allows for eight modules to be installed which then connect to the valves. The eight modules used in this application were NI 9481 SPST relay modules to

switch the on/off signal to the valves. Each module contains 4 SPST switches for a total of 32 available switches. As with the manual switches, 120 VAC is run to the input side of each relay and is connected to the valve from the output side. The LabVIEW program, called Solenoid Control.vi, uses a visual representation of the system to show the valves being opened and closed. Using a visual representation of the system is very beneficial to the user because they can directly see what they are doing with the system at all times. This helps the user to understand exactly how the system is operating and how it works. A picture of this program is shown in Figure 10. The emergency stop button on the switchbox will stop all the valves in both LabVIEW control and manual control. The full LabVIEW programming schematic and a larger image of the user interface is shown in the supplemental information.

The Solenoid Control program directly interfaces with the cDAQ system. When a user clicks a button on the program, the signal is sent to the correct relay on the module plugged into the cDAQ. This activates the solenoid. In the program, the buttons activated will be indicated by a light, a color change, or both. The buttons labeled “purge” change color indicating that they are activated. When one of the entry valves is turned on, the button changes color and the light to the right of the button comes on. For all valves connected to the Main Entry valve, the light on the main line will also activate, showing that process gas is present in this line. For the separate stannane and boron trichloride valves, the light on the line activates. For the Main Entry, Stannane Chamber Entry, and Boron Trichloride Chamber Entry valves, the individual light associated with that line will come on and the larger light on the entry line will come on. Buttons for the larger valves on the system are also equipped with a light that comes on when the button is activated.

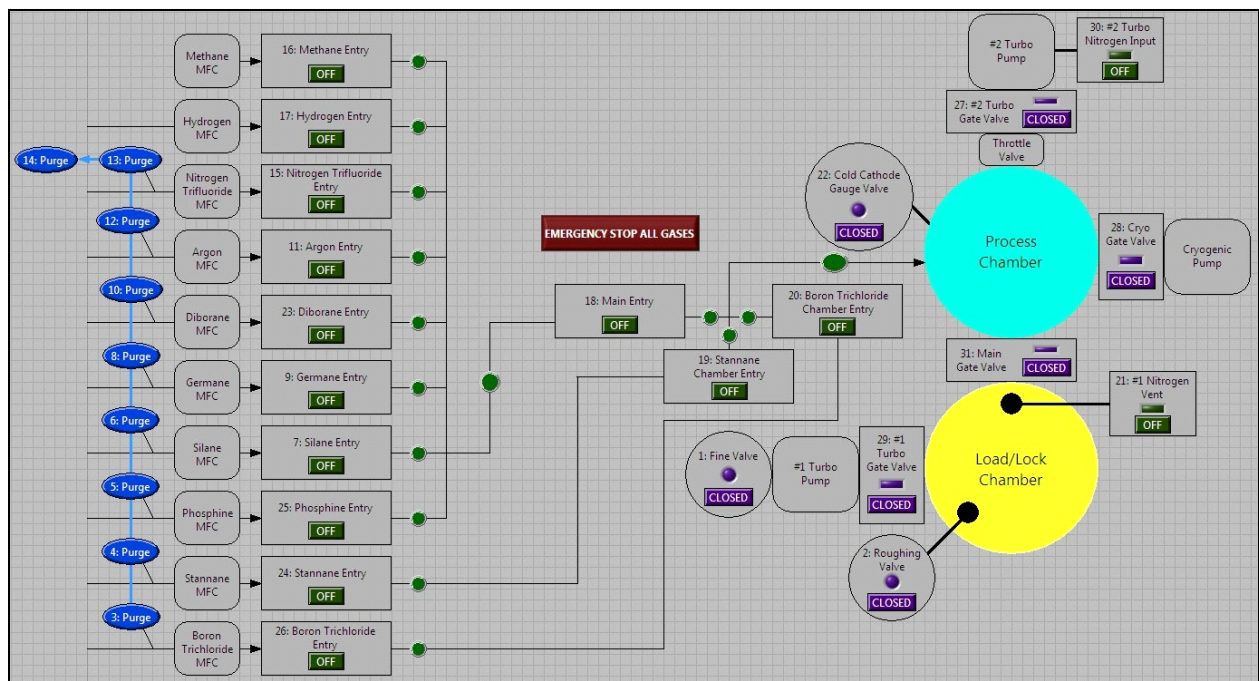


Figure 10: LabVIEW program Solenoid Control.vi user interface.

When performing a deposition, the valves are turned on in order starting from the chamber. For example, if a silane deposition is performed, the Main Entry valve would first be activated, and then the Silane Entry valve. After this, the mass flow controller for Silane would be set to the appropriate value. The manual turn bellows valve directly after the silane regulator would then be opened, and the regulator would turn on.

To switch between LabVIEW control and manual control, a switchbox was built to switch power supply between the two control schemes, as shown in Figure 11. Power is first routed through the switchbox emergency stop button, which serves as an emergency stop to all the solenoids. Then, a three-way switch is used to select the mode of control. On the left is computer control, and on the right is switchbox control. The middle position is off, which allows one system to be completely disengaged before another system is engaged. The LabVIEW and switchbox wires join after the relay modules and switches before going to the valves as shown in Figure 12. This is accomplished using the solenoid signal junction box. A wiring diagram for the

junction box is shown in Figure 14. The wires from the switchbox come in on the left side. On the right side, the wires from the cDAQ relay enter and join the wires from the switchbox. This signal is then sent to the solenoids through the bottom of the switchbox. The group of wires at the top of the box, labeled in red, provides power to the cDAQ relays from the emergency stop button on the switchbox. All wires from all sides of the box are labeled with the appropriate solenoid number. The lines are also labeled where they connect to the solenoids, the cDAQ, and the switchbox.

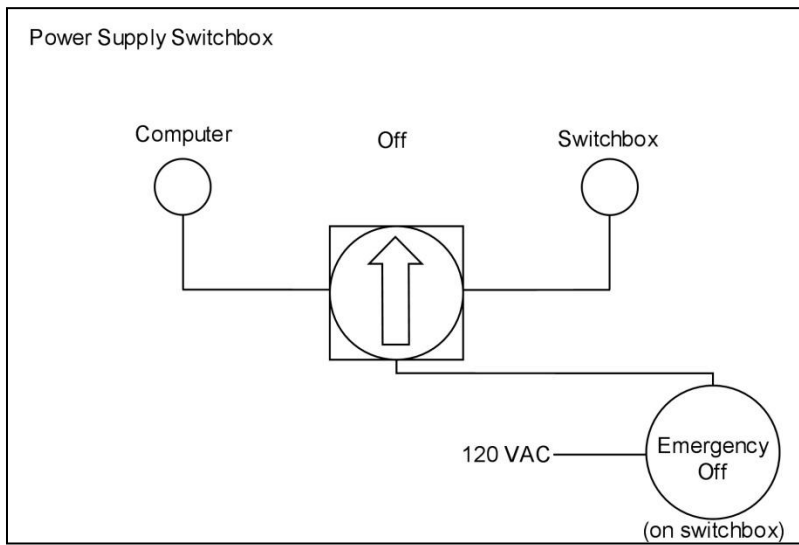


Figure 11: Schematic of the power supply switchbox.

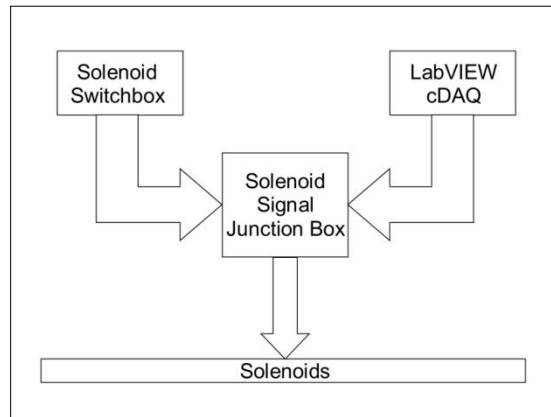


Figure 12: Diagram showing signal progression from control schemes.

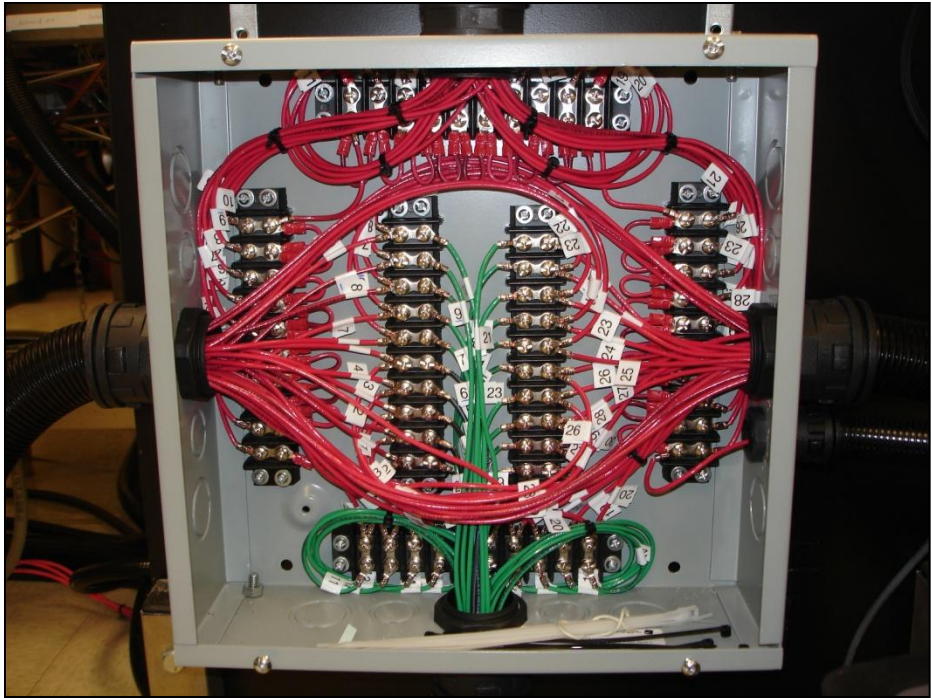


Figure 13: Image of the solenoid signal junction box.

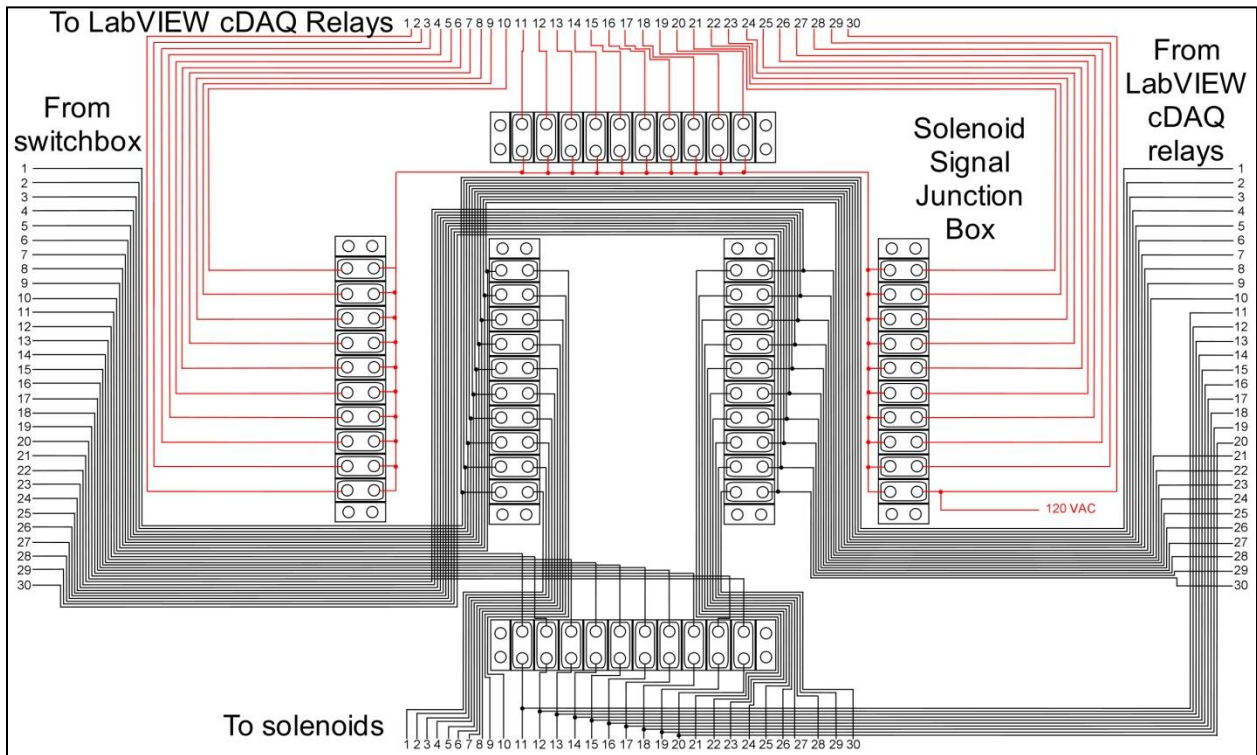


Figure 14: Connections inside the solenoid signal junction box wiring diagram.

3.1.3: Safety Features

Because of the system's use of hazardous gases, several safety features have been added to alert users to the possibility of a dangerous situation. Sniffers, which are on an uninterrupted power supply, have been installed to sample the air at several different locations. If a hazardous gas is detected, an alarm will sound and at the same time the hazardous gas will be shut off at the regulator. This is accomplished by using two relays inside the sniffers. The first relay used is a normally closed relay that opens when a hazardous gas is detected. These relays are connected in series to the main building alarm. When an open circuit is detected, the building alarm sounds. The second relay used is normally open. These relays are connected in parallel to the hazardous gas alarms installed in the lab, hallway, back chase area and outside near the gas farm. In each location are two alarms, one red and one white, to indicate the type of gas leak detected. A red alarm indicates a combustible gas (hydrogen, methane, or stannane) while a white alarm indicates a toxic gas (phosphine, diborane, nitrogen trifluoride, boron trichloride, silane, or germane). The sniffer relays are supplied by 24 VDC from an uninterrupted power supply. When one relay closes, 24 VDC is supplied to each of the alarms. At the same time, the shutoff valve is actuated from open to closed, stopping the flow of gas right after the regulator. The shutoff valves can also be manually actuated by a switchbox on the main system table. Connections to the alarms are made in the sniffer alarm box. Connections to the shutoff valves are made in the high-pressure pneumatic junction box. Wiring diagrams for these junction boxes are shown in Figure 16 and Figure 18.

The Sniffer and Alarm Box is shown in Figure 15 and Figure 16. On the left side of the figure is the power supply to the normally open sniffer relays. These lines supply the 24 VDC necessary to run the local alarms should one of them close. Each line returns from the sniffer and is connected to the appropriate alarm wire through the terminal on the right side of the box. The

lines are also connected to Wire 1, which runs outside to the High Pressure Pneumatic Junction Box (shown in Figure 18) to control the high-pressure shutoff valves for the gases equipped for them. On the bottom, the lines return from the gas shutoff switchbox through Wire 3 and actuate the local alarms. The gas shutoff switchbox is a small switchbox interrupting the flow of power to the high-pressure pneumatic shutoff valves so that they can be controlled manually.

The High-Pressure Pneumatic Junction Box is shown in Figure 17 and Figure 18. Inside this box, relays and solenoids are used to control the switching of the high-pressure pneumatic shutoff valves located just after the gas regulators. Wire 1 carries the sniffer alarm signal to the junction box and connects to the relays. This signal is what actuates the relay and when detected causes the relay to change connections. Wire 2 carries the signal inside to the gas shutoff switchbox, along with two wires from Wire 4. From the gas shutoff switchbox, the signal is carried through Wire 3 to the sniffer alarm box. This then actuates the local alarms. From the individual switches, Wire 4 carries the signal back to the high-pressure shutoff valves in the High-Pressure Pneumatic Junction Box. The lines from Wire 4 actuate the solenoids. Since no boron trichloride bottle is currently connected, this solenoid has been left disconnected, and can be connected when a bottle is ordered.

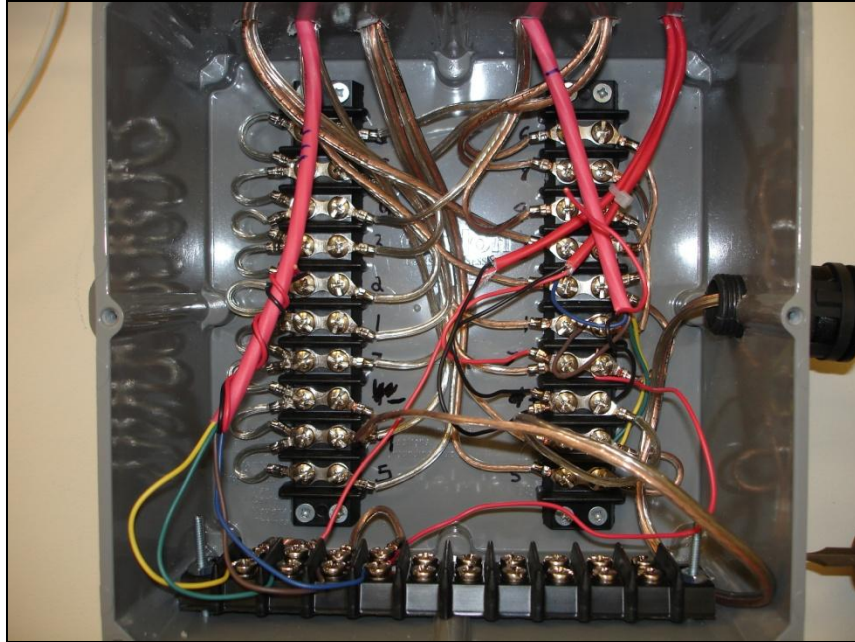


Figure 15: Image of the sniffer and alarm box.

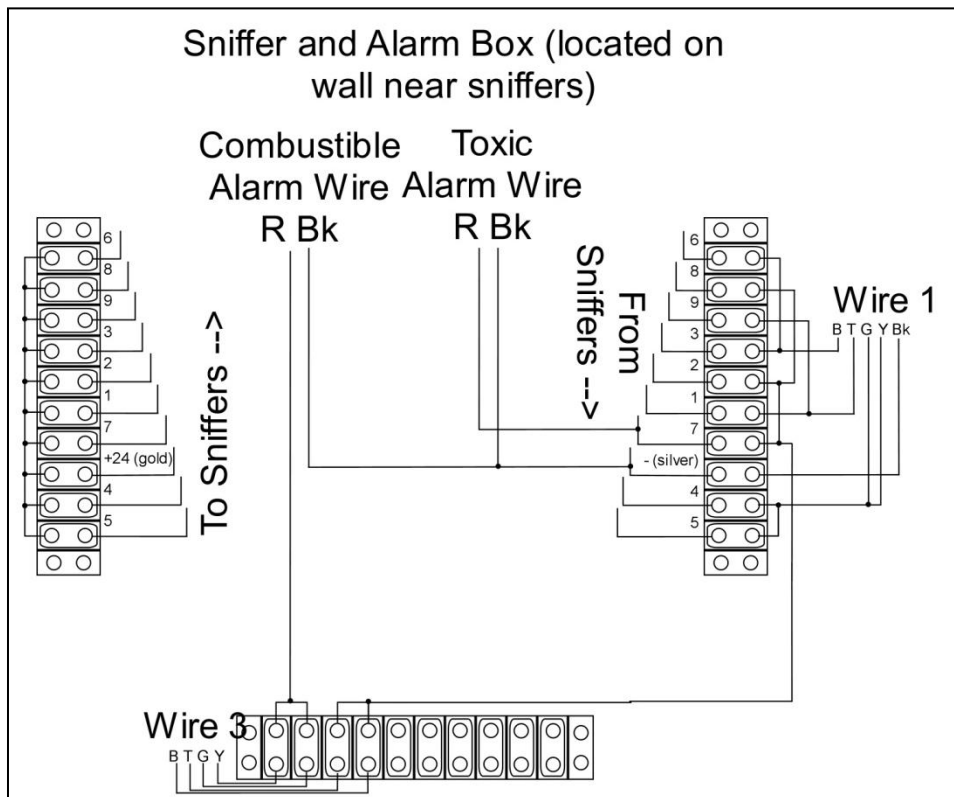


Figure 16: Connections inside the sniffer alarm box.



Figure 17: Image of the high-pressure pneumatic junction box.

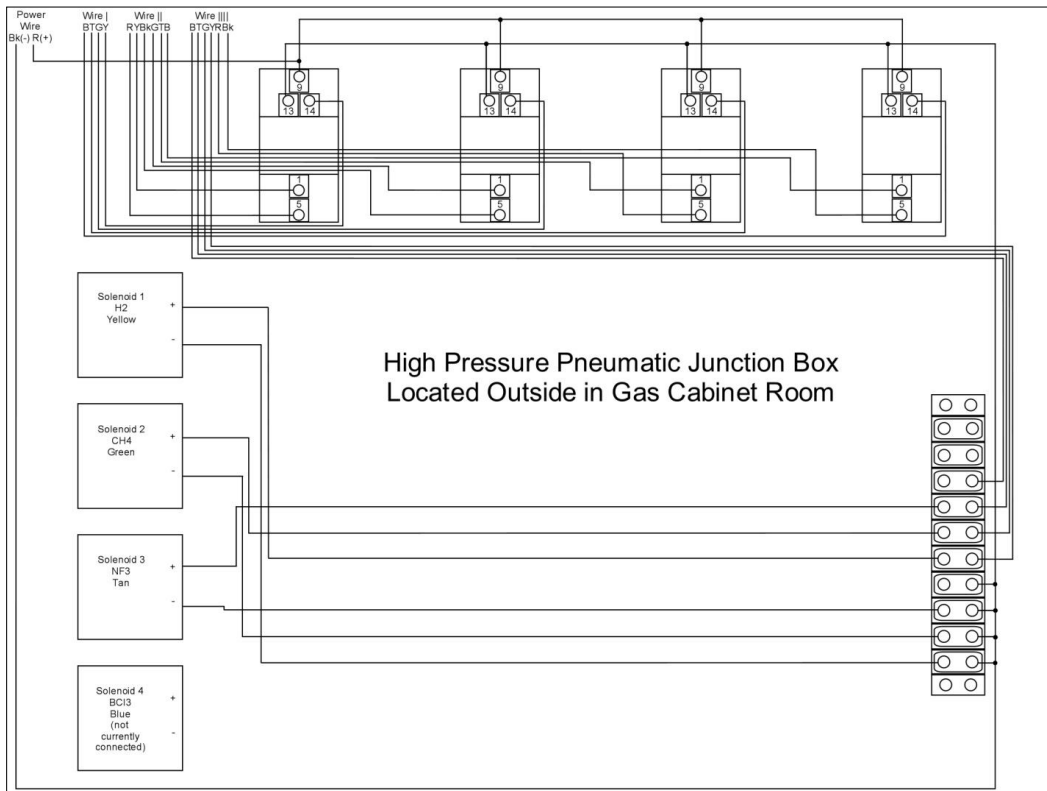


Figure 18: Connections inside the high pressure pneumatic junction box.

An exhaust monitoring system as shown in Figure 19 has also been installed to alert the user to a possible exhaust failure in the system. The exhaust is monitored at three points currently: the GRC cabinet, the gas cabinets, and the mass flow controller exhaust hood. The exhaust detectors are equipped with a normally-closed relay that opens when the exhaust flow falls below an acceptable point. They are supplied with 24 VDC from an uninterrupted power supply. When the exhaust flow fails, this relay opens. The relays inside the exhaust monitoring box detect this open circuit and simultaneously turn on the neon light(s) indicating the site of the exhaust leak and the strobe light to alert the user. A wiring diagram for the exhaust monitoring box is shown in Figure 20.

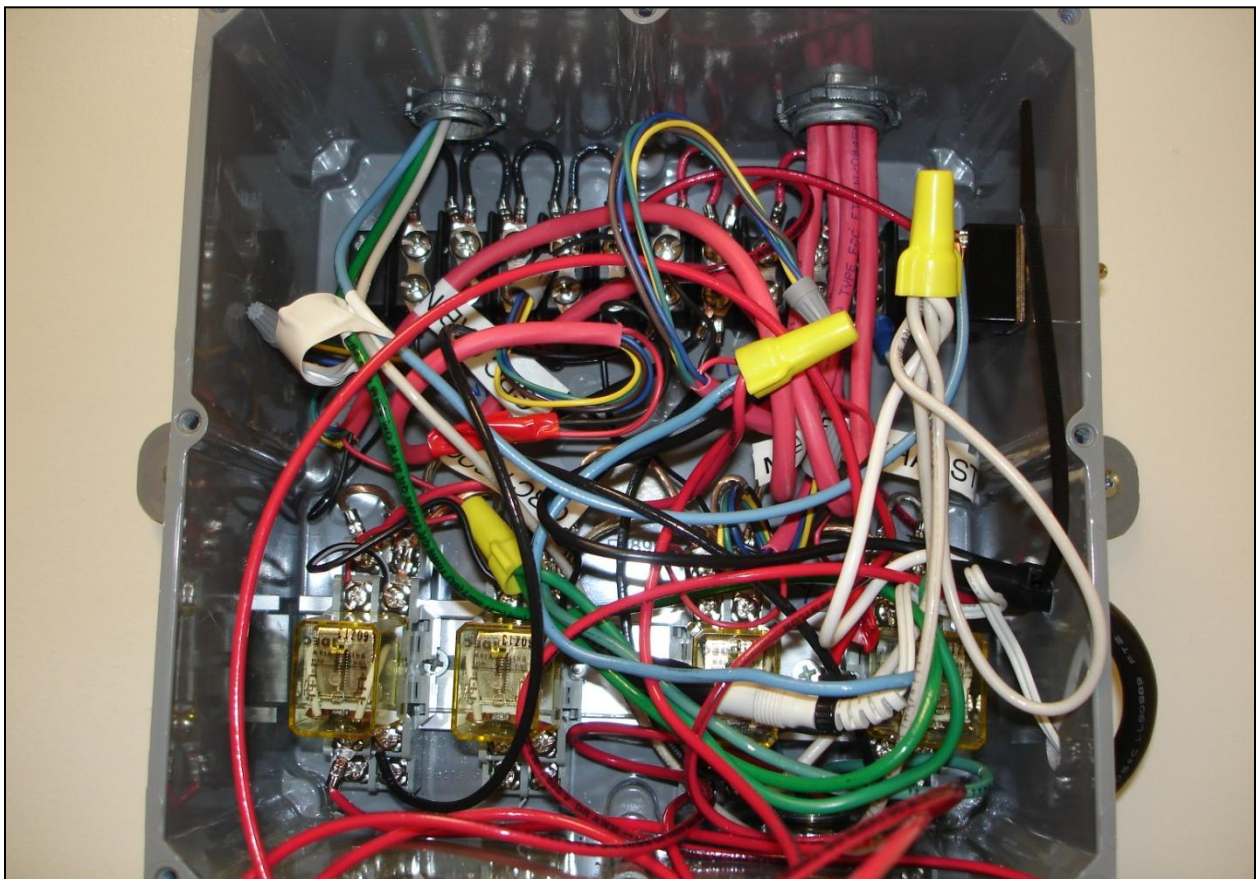


Figure 19: Image of the exhaust monitoring box.

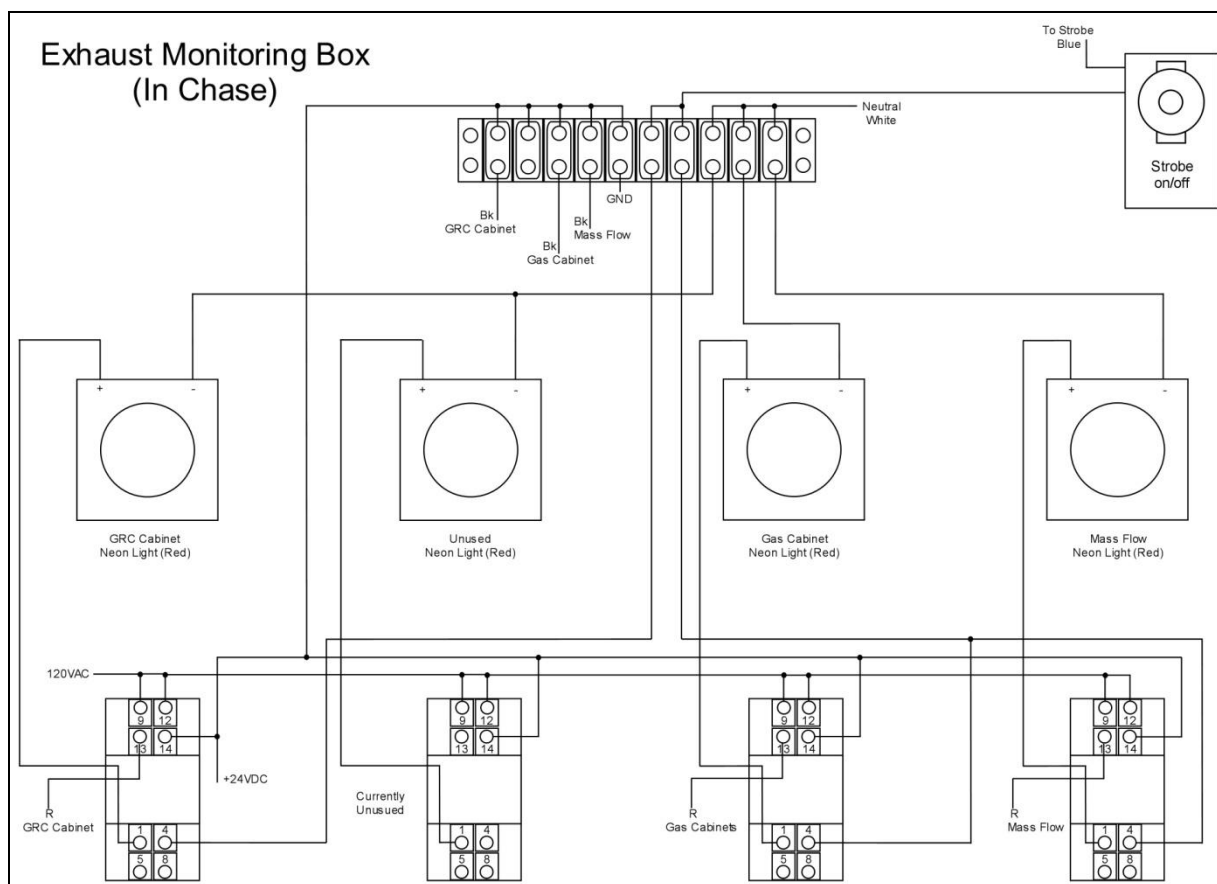


Figure 20: Connections inside the exhaust monitoring box.

3.1.4: Status of the UHV-PECVD System

The main construction period of the system ended in fall 2011. Though small enhancements are being made to the system as they are needed, the system is fully ready for use in deposition processes. Because of the high expectations of the University of Arkansas in regards to safety, the system is currently undergoing evaluation by the Environmental Health and Safety department. It is expected that the system will be fully ready for depositions by fall of this year, 2012. For this reason, a smaller PECVD system in Room 350B was used for preliminary carbon depositions.

3.2: Overview of Single-Chamber CVD System

A small CVD system in room 350B of the ENRC as shown in Figure 21 was used for performing preliminary depositions. Dr. Husam Abu-Safe, the lab manager, performed the scheduled depositions. A schematic of the CVD system is shown in Figure 22. The system consists of a single chamber equipped with a mechanical pump, turbomolecular pump, throttle valve, heating stage, 13.56 MHz RF source for plasma enhancement, and several process gases including hydrogen and methane. The process gases enter from the bottles through various valves and mass flow controllers. They deposit on the substrates mounted face-down on the substrate heating stage. The plasma is struck using the RF source and matching network. The pressure is maintained through the use of a throttle valve and measured using a capacitance manometer. After deposition, the gases are pumped out using the turbo and mechanical pumps.



Figure 21: The single-chamber CVD system in room 350B of the ENRC.

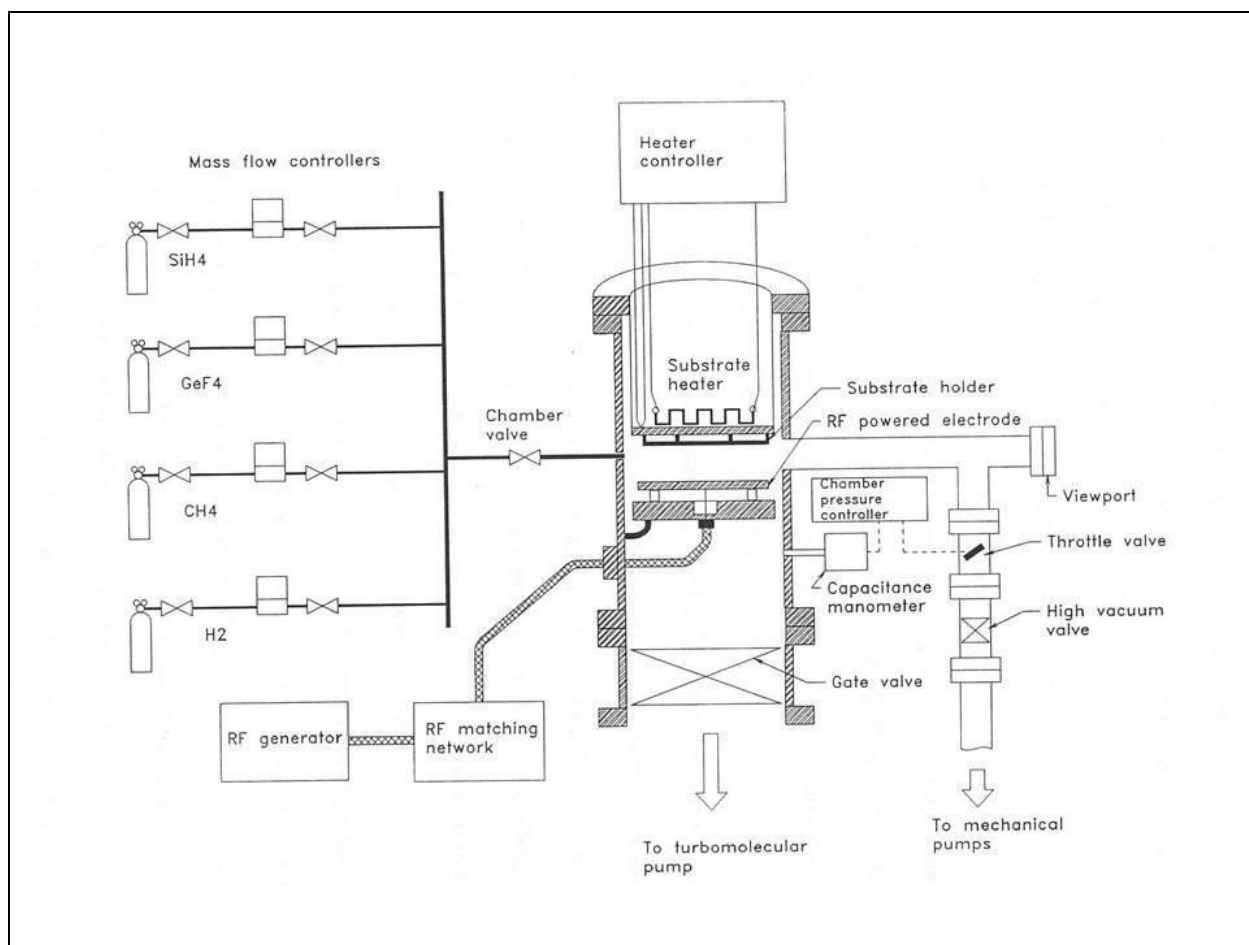


Figure 22: Schematic of the single-chamber CVD system [46].

3.3: Experimental Procedures

The parameter space investigated was chosen due to the limitations of the CVD system available and after thorough review of current graphene literature. It was decided that two parameters, temperature and duration, would be investigated in a series of nine experiments. In each experiment several variables were held constant. The pressure was held at approximately 200 mTorr, and the plasma power at 25 W. The flow rates of hydrogen, argon, and methane were held constant at 40 sccm, 40 sccm, and 10 sccm respectively. The temperature was varied from 280°C to 480°C and the time was varied from 1 minute to 10 minutes. One additional run, run 2,

was performed at 280°C for 30 seconds at a pressure of 500 mTorr and with power and flow rates the same. The matrix of experiments performed is shown below in Table 4.

Run Identification Number	Temperature (°C)	Time (minutes)
1	480	10
2	280	0.5
3	280	10
4	280	5
5	380	5
6	480	5
7	480	1
8	380	1
9	280	1
10	380	10

Table 4: Master run list of experiments performed

Depositions were performed on several substrates. High-purity nickel foil (Puratronic 99.994% pure, 0.1mm thick, Alfa Aesar), high-purity copper foil (Puratronic 99.9999%, 0.1mm thick, Alfa Aesar), glass slides, and silicon wafer pieces were used in all depositions. Runs 6, 7, 8, 9, and 10 were also performed on both copper and nickel TEM grids using a grid holder, as seen in Figure 23. Additionally, run 6 was repeated once on a carbon-coated copper TEM grid. The nickel and copper foils were cut into 1cm x 2.5cm pieces. The foils were then cleaned in an acetone bath at 40°C for 10 minutes followed by a methanol bath at 40°C for 10 minutes, both under sonication. They were dried by nitrogen blowing.

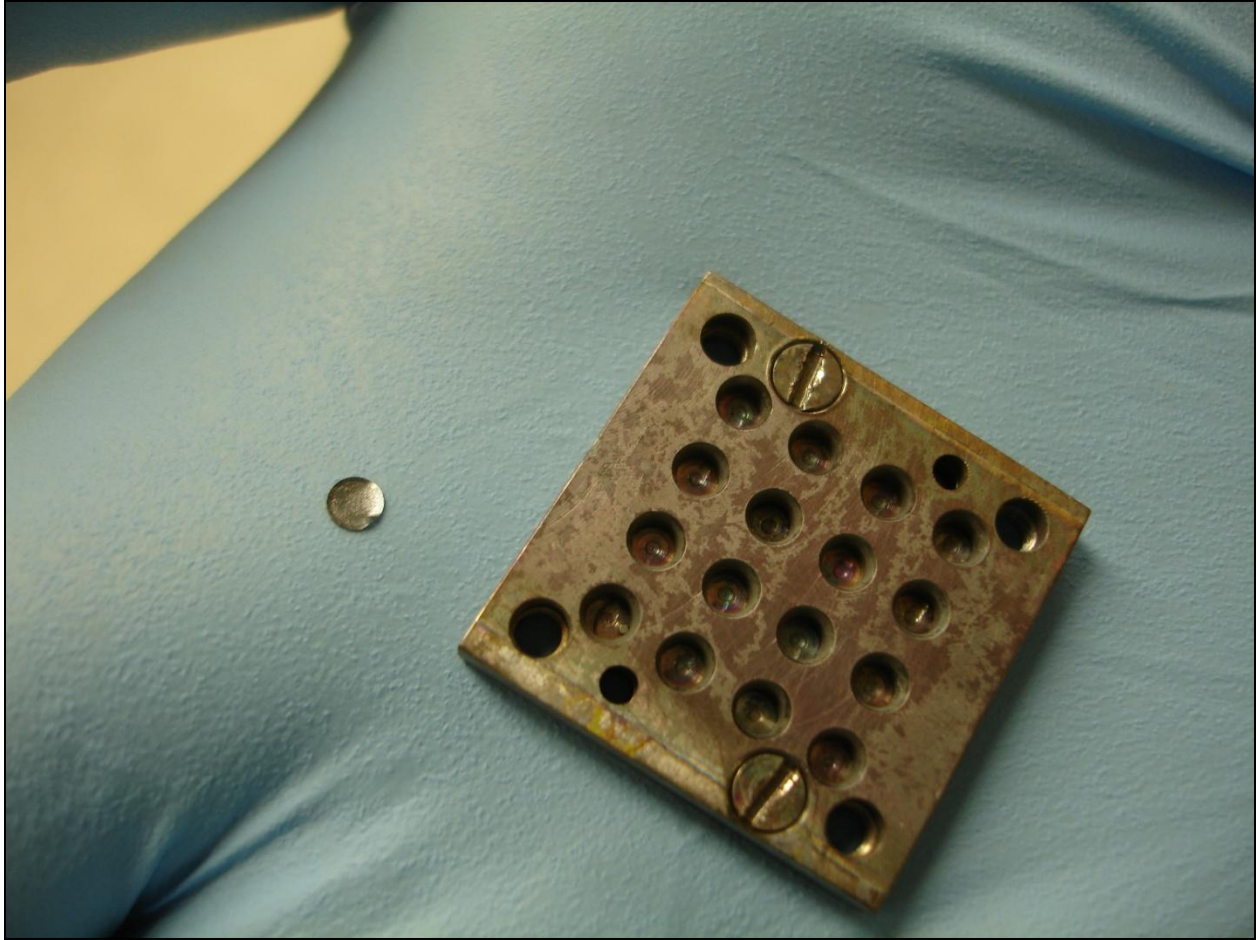


Figure 23: Nickel TEM grid (left) and TEM grid holder used in growth process.

The process for growth was as follows: First, the substrates were loaded into the substrate holder, which is then placed upside down on the heating stage. The heater assembly is then placed in the chamber. The chamber is then pumped down to the 10^{-5} Torr regime while the heating stage is heated to the desired temperature. Once the temperature stabilizes and the pressure reaches the high vacuum regime, the process gases are then set to the desired flow and introduced. The pressure in the chamber is then adjusted using the throttle valve to the desired deposition pressure. Once all the deposition parameters are stable, the RF source is turned on and the plasma is activated. The deposition time was recorded from the time the plasma struck to the time it was turned off at the end of the deposition period. After this, the gases were stopped and

the system was allowed to cool to at least 70°C. The samples were then unloaded and placed into labeled boxes.

Chapter 4: Results and Discussion

All films grown in the small CVD chamber were characterized using optical transmittance and Raman spectroscopy. Scanning electron microscopy, transmission electron microscopy, and energy-dispersive x-ray spectroscopy (EDX) were also performed on select samples for investigation of structure and elemental analysis. Raman spectroscopy was performed using a Horiba Jobin Yvon HR800 UV commercial spectrometer. The laser wavelength was 633 nm, spot size 1 μm , hole size 300 μm , power 5 mW, 600 grating. The scan duration (shutter time) was 15 seconds and the intensity of the signal was measured in counts. Transmittance was performed using an original system built by students at the University of Arkansas. The spectrum taken was from 400 nm to 1100 nm with light intensity 50 W. TEM imaging was performed with an FEI Titan at 200kV, and SEM imaging with an FEI Nova Nanolab. Raman data were smoothed to provide easier peak identification.

All samples, except for samples from run 2, had visible deposition on the copper and nickel foils. Deposition on these substrates can be seen in Figure 24 and Figure 25. Longer runs at higher temperatures, for example run 6, showed deposition on the glass and silicon substrates, though shorter and lower-temperature runs did not. The film deposition on the silicon substrates can be seen in Figure 26, and on the glass substrates in Figure 27. The deposited films are adhered to the substrate and cannot be scratched off. Therefore, it is evident that they are crystalline and not polymeric.

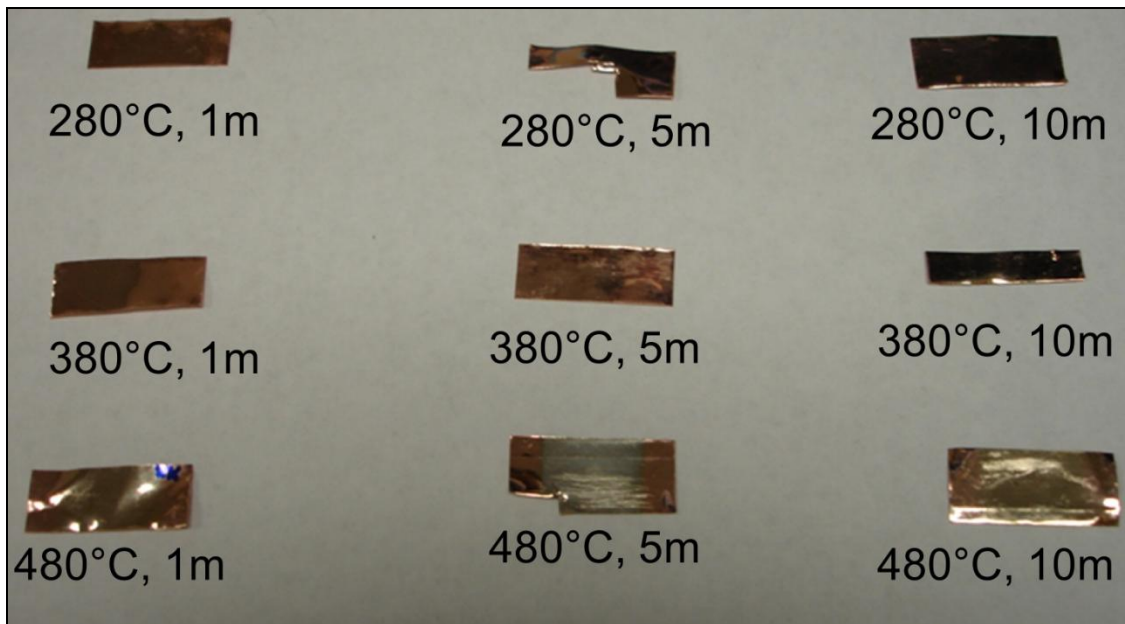


Figure 24: Image of deposition on copper substrates.

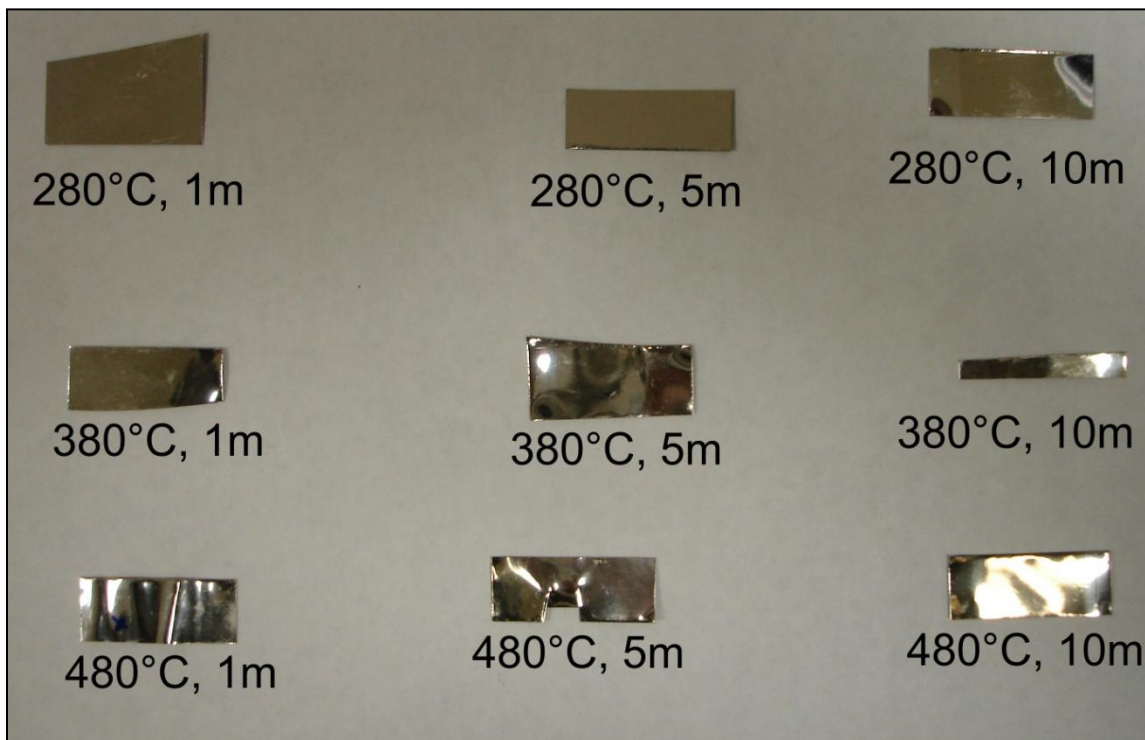


Figure 25: Image of deposition on nickel substrates.

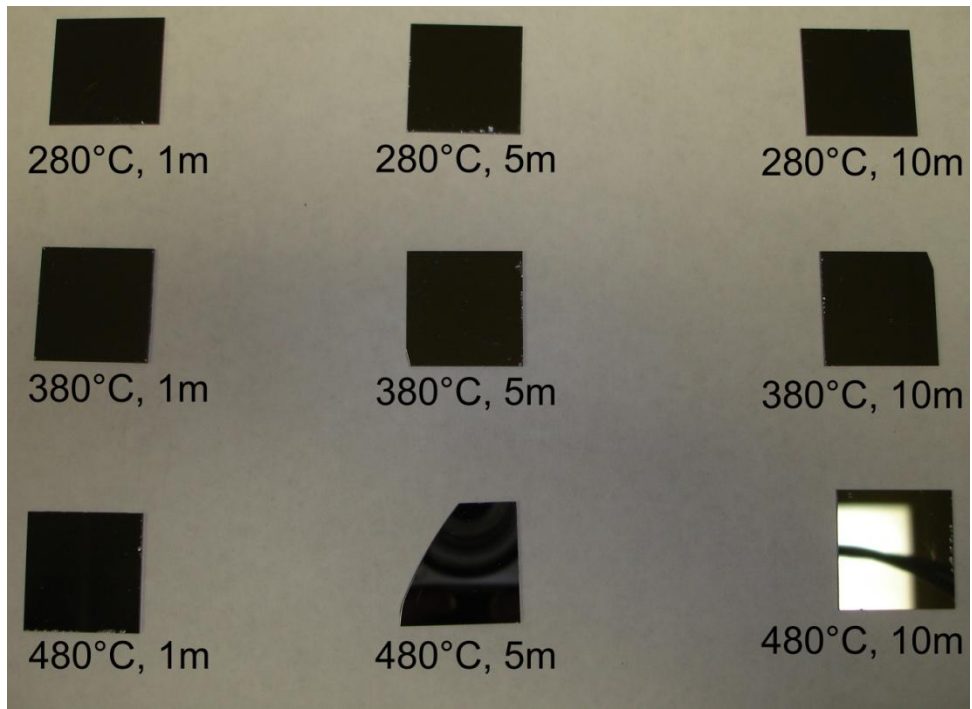


Figure 26: Image of deposition on silicon substrates.

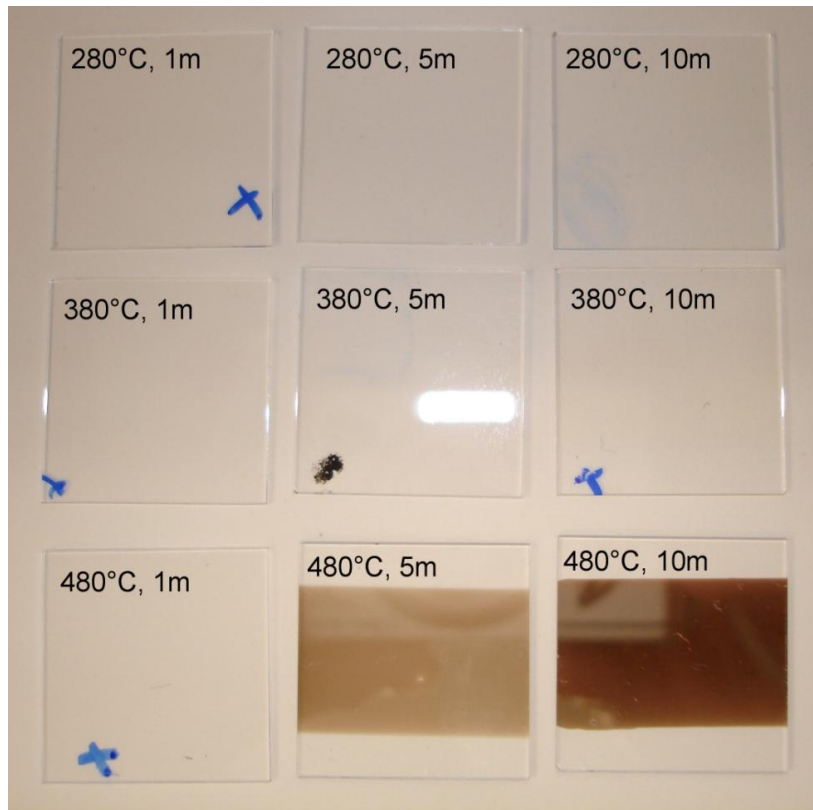


Figure 27: Image of deposition on glass substrates.

4.1: Results of Optical Transmittance

To achieve percent transmittance, the transmittance of a pure glass sample and of the samples with deposition was obtained. The transmittance of the sample was then divided by the transmittance of the glass and the data were smoothed. Data were obtained in the visible range from 600 to 1100 nm using a home-built setup with 80 W lamp power.

In many cases, the percentages found were above 100%. Data were taken multiple times from a pure glass sample and compared to find measurement error. It was found that the largest error in these samples was 4.4%, indicating a small percentage of error in the measurements.

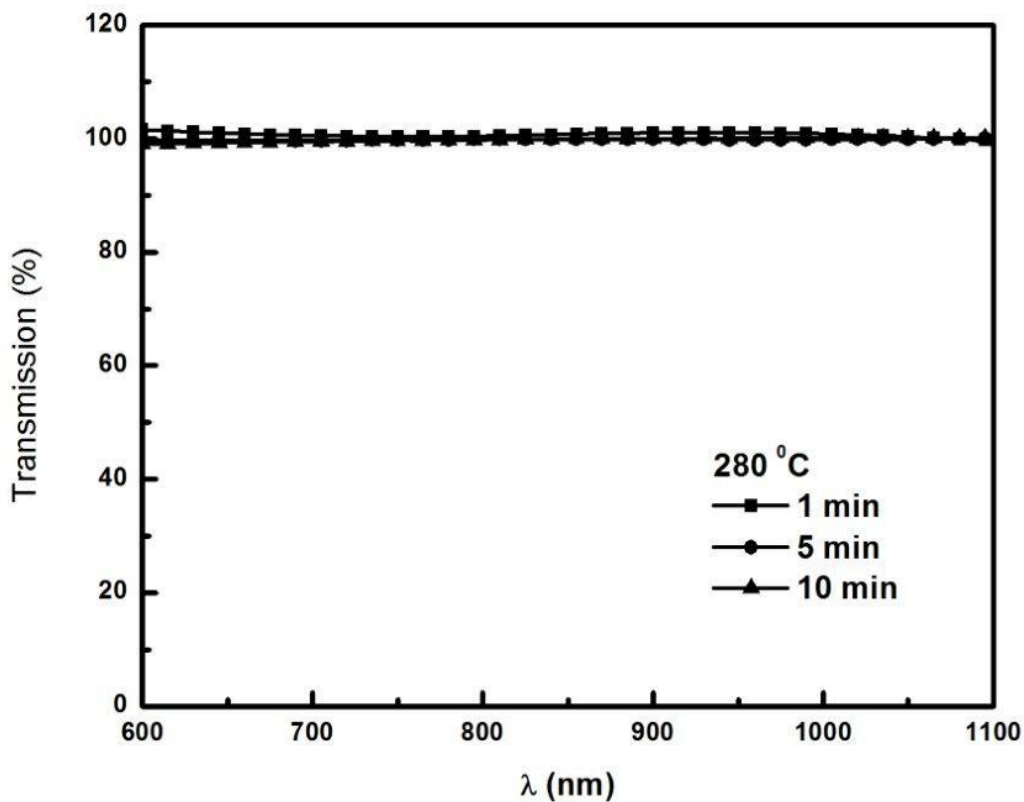


Figure 28: Transmittance of samples grown at 280°C for 1, 5, and 10 minutes.

The results for depositions performed at 280°C are shown above in Figure 28. Though these numbers are slightly above 100%, they are fairly consistent within the data set. Fluorescence can also be occurring in this region. With increasing time, the transmittance decreases, indicating a thicker film present.

Results for depositions performed at 380°C are shown below in Figure 29. These percentages are also above 100%, but within the margin of error. Consistent with the results at 280°C, the overall transmittance decreases with increasing time, indicating a thicker film.

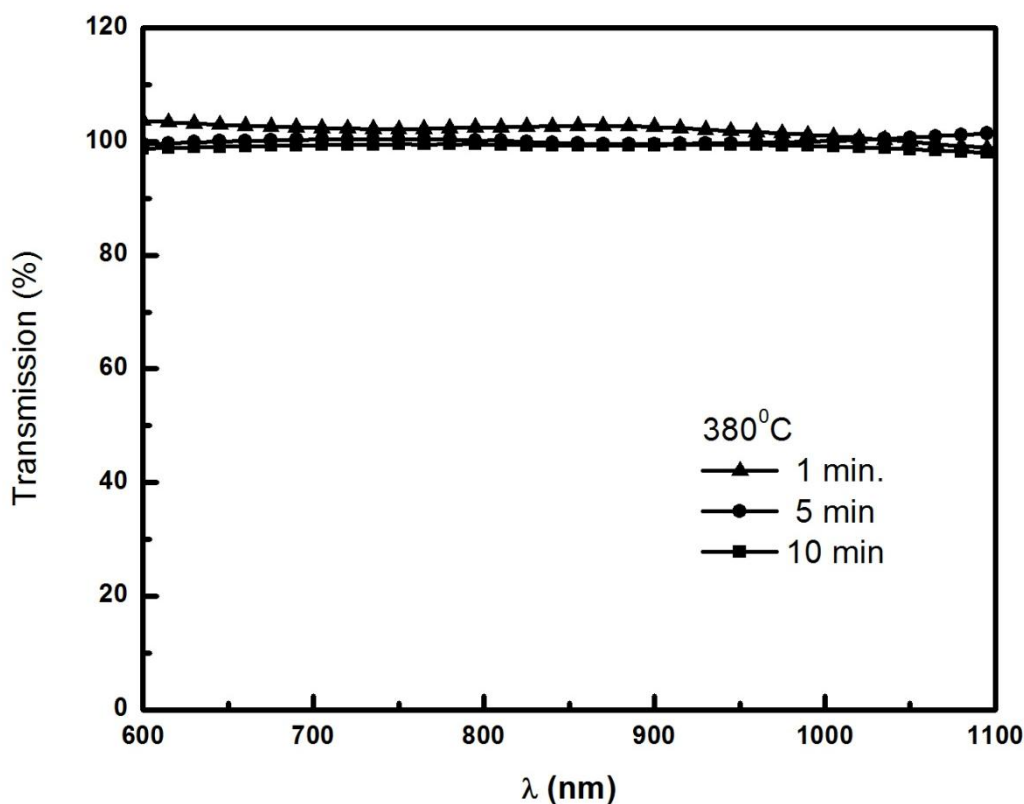


Figure 29: Transmittance of samples grown at 380°C for 1, 5, and 10 minutes.

Results for runs performed at 480°C can be seen below in Figure 30. These results look overall quite different than previous results. The films on these slides, however, look thicker to the naked eye than films grown at lower temperatures. As seen at the other temperatures, there is an overall decrease in transmittance with increasing growth time. For the growth performed at 5

minutes, the dip at 600 nm is also seen, however it is not apparent in any of the other data at this temperature.

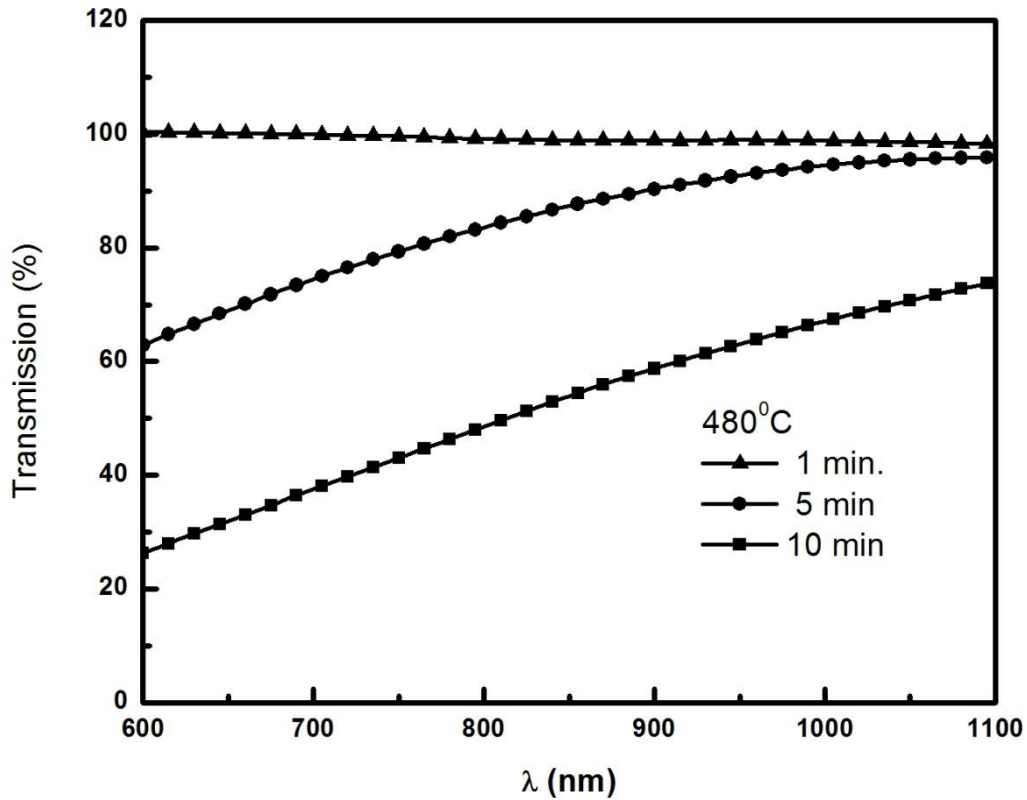


Figure 30: Transmittance of samples grown at 480°C for 1, 5, and 10 minutes.

Comparison of transmittance across different temperatures is also useful to investigate. Below in Figure 31 it can be seen that increasing temperature leads to an overall decrease in transmittance. This is also confirmed in Figure 32 and Figure 33. The transmittance of samples run at 280°C and 380°C appears close in this case, but it can be seen that the transmittance of the 280°C sample is normally slightly higher than of the 380°C. This is also supporting evidence of a thicker film forming at higher temperatures.

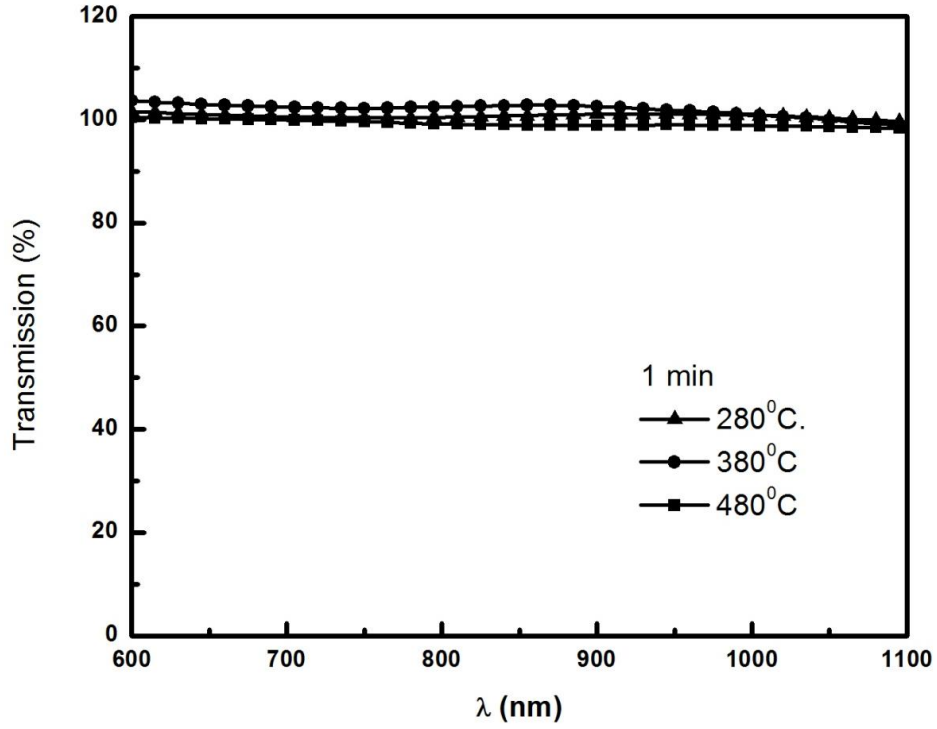


Figure 31: Transmittance of runs performed for 1 minute at different temperatures.

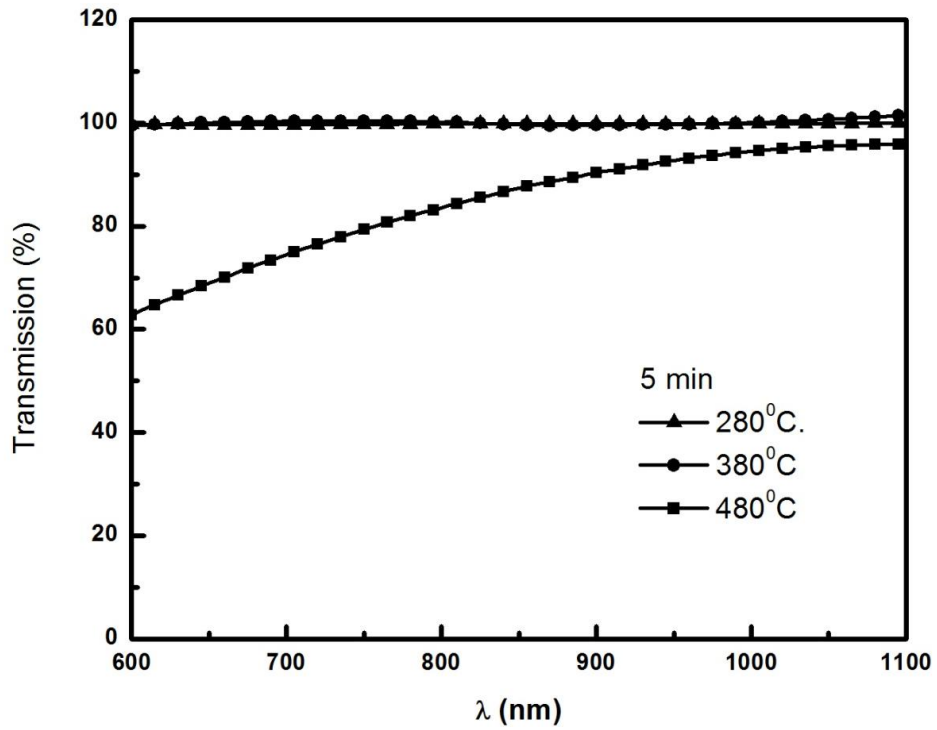


Figure 32: Transmittance of runs performed for 5 minutes at different temperatures.

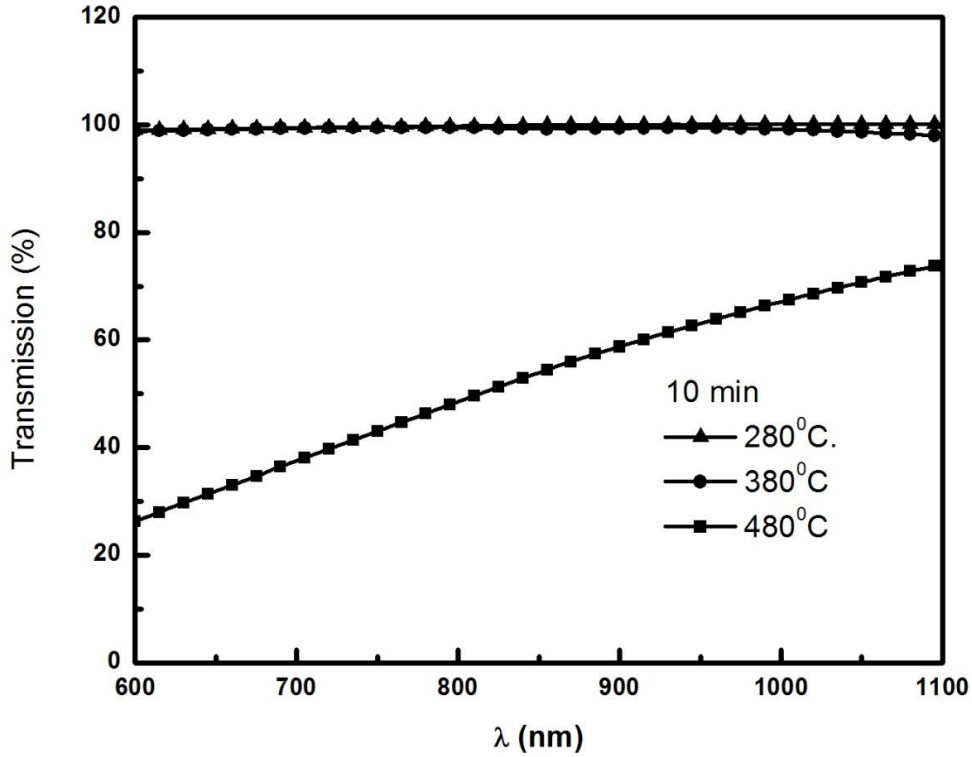


Figure 33: Transmittance of runs performed for 10 minutes at different temperatures.

4.2: Results of Raman Spectroscopy

As can be seen in Figure 34, Raman spectroscopy of the plain glass substrate shows several peaks of low intensity from 1000 cm^{-1} to 1700 cm^{-1} . There is an intense peak at 1111 cm^{-1} , another at 1372 cm^{-1} , and another at 1477 cm^{-1} . This spectrum will be used to compare the sample spectra, as the analyzed samples were grown on glass. An additional peak at 1984 cm^{-1} was also seen. The Raman spectrum of borosilicate glass has been studied in detail. Several peaks are seen in the spectrum, two of the highest being at approximately 1100 and 1500 cm^{-1} [47].

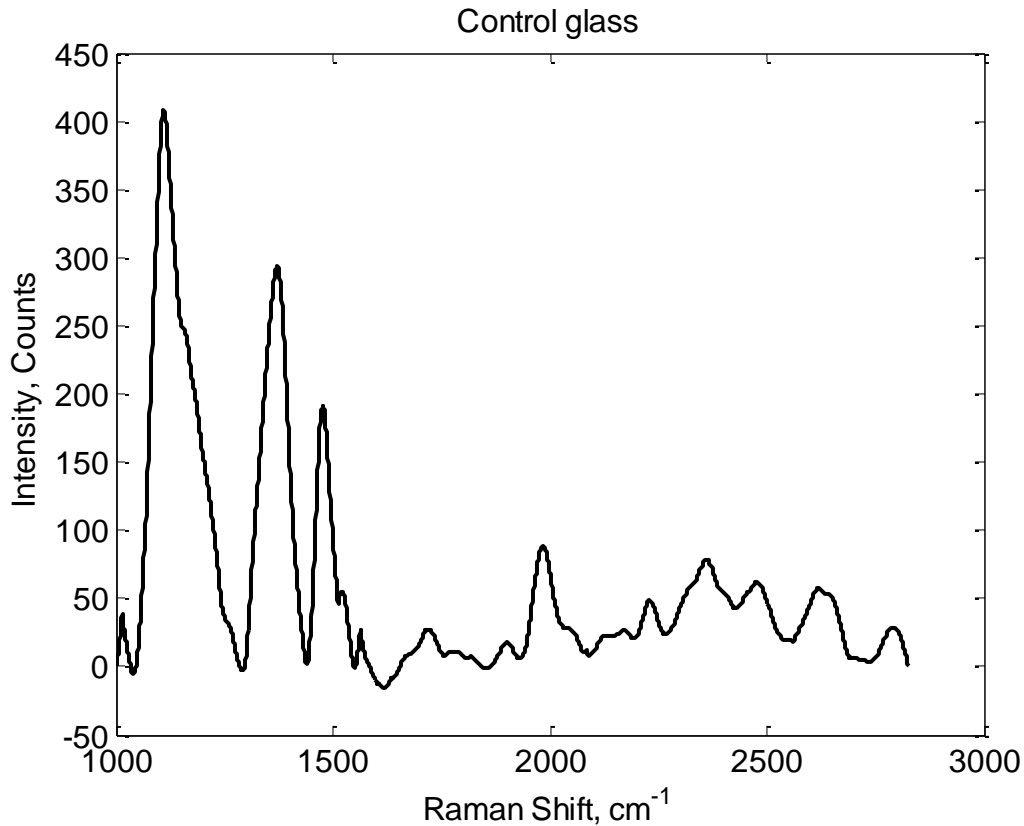


Figure 34: Raman spectrum of plain glass substrate.

The Raman spectra of amorphous carbon and diamond are also of interest due to the possibility of amorphous and diamond structures in the samples. The most prominent Raman peak in diamond is located at approximately 1330 cm⁻¹. The Raman spectrum of amorphous carbon is also quite close to that of graphene and graphite. Amorphous and nanocrystalline samples exhibit both the G and D peaks [48].

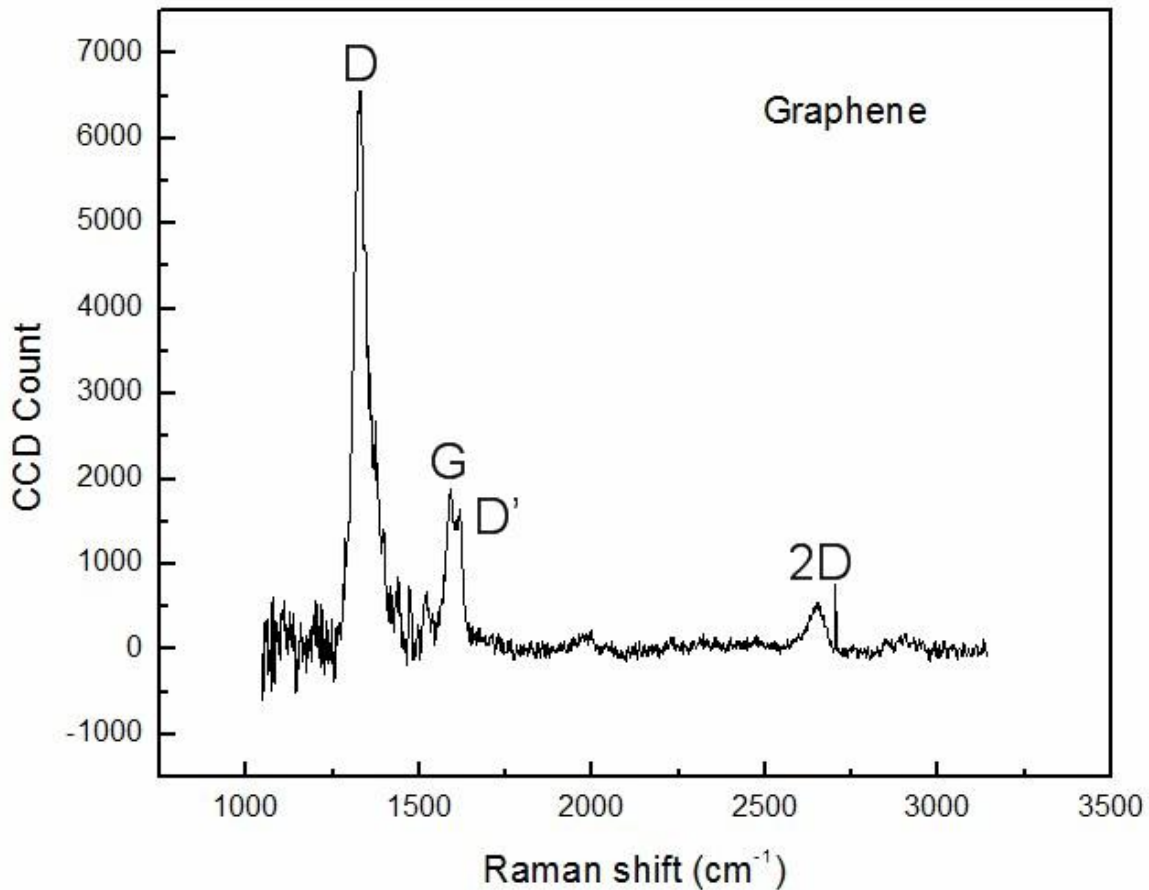


Figure 35: Raman spectra of graphene provided by Army Research Laboratories. Used with permission from Asmaa Elkadi.

The Raman spectrum of a graphene sample on a silicon substrate provided by Army Research Laboratories was also obtained as shown in Figure 35. The D (1360 cm^{-1}) and G (1580 cm^{-1}) peaks can be clearly seen along with a 2D (2700 cm^{-1}) peak. This indicates that this Raman system can be used to evaluate graphene. A small peak slightly below 2000 cm^{-1} also appears, consistent with the clear glass sample shown above.

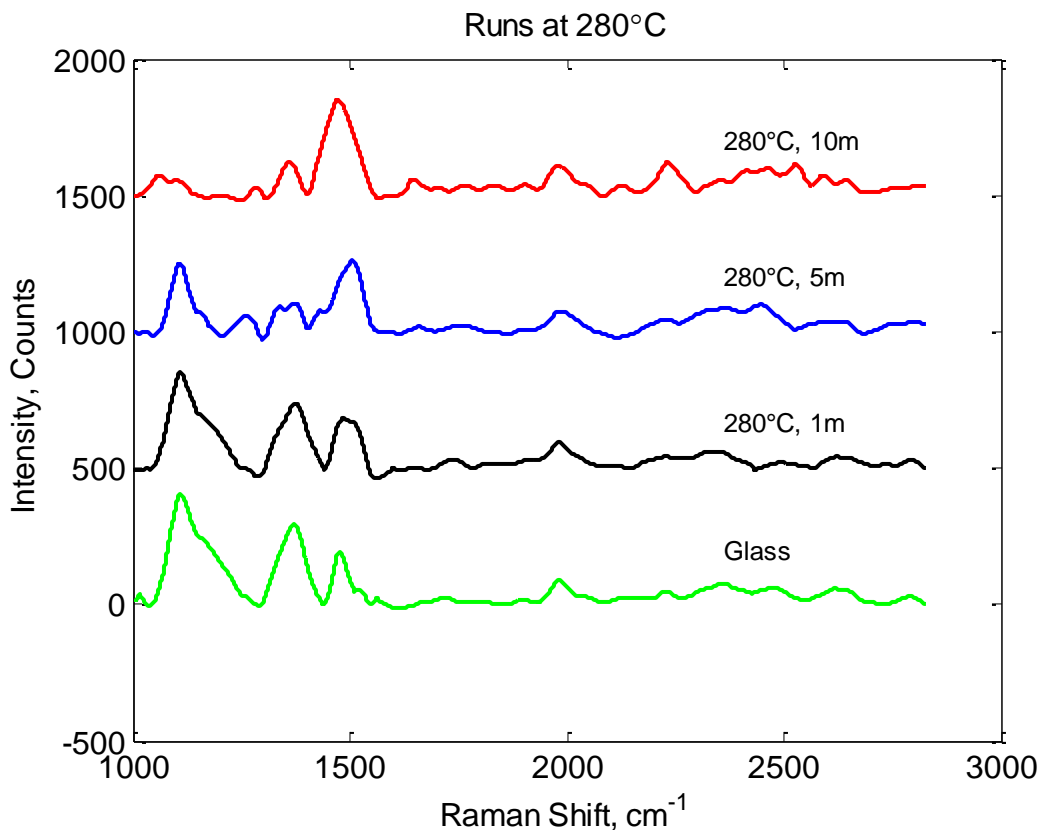


Figure 36: Raman spectra of runs performed at 280°C for 1 minute, 5 minutes, and 10 minutes as compared to blank glass.

The results of samples run at 280°C for 1 minute, 5 minutes, and 10 minutes are shown above in Figure 36. At 1 minute, there are three distinct peaks at 1111, 1375, 1495 cm^{-1} . As the growth time increases, the intensity of the peak at 1111 cm^{-1} falls and the intensity of the peaks at 1375 and 1495 cm^{-1} increases. There is also a slight shift in the peaks. At 5 minutes, the third peak has shifted to 1508 cm^{-1} and at 10 minutes back to 1475 cm^{-1} . The peak at 1375 cm^{-1} also shifts slightly to a wider peak centered at 1363 cm^{-1} for 5 minutes and to 1361 cm^{-1} for 10 minutes. The peak at 1111 cm^{-1} , however, does not shift and completely disappears for the 5 minute growth. Additionally, a low-intensity peak is seen at 1980 cm^{-1} for all three samples, as was seen in the glass. The intensity is consistent throughout all three samples.

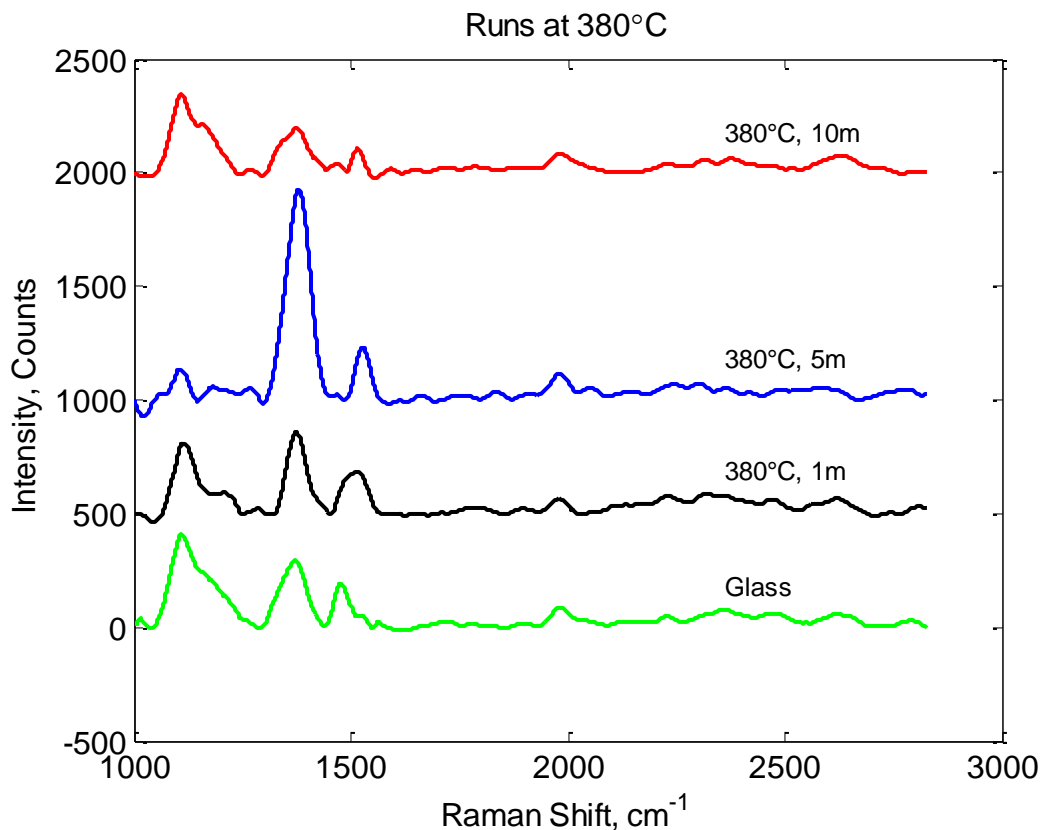


Figure 37: Raman spectra of runs performed at 380°C for 1 minute, 5 minutes, and 10 minutes as compared to blank glass.

The Raman spectra for samples grown at 380°C are shown above in Figure 37. The spectrum at 1 minute of growth shows 3 distinct peaks at 1111 cm^{-1} , 1375 cm^{-1} , and 1515 cm^{-1} . The five minute growth shows an increase in intensity of the second peak which is also slightly shifted to 1380 cm^{-1} . The intensity of the third peak is slightly higher and is shifted to 1580 cm^{-1} . The intensity of the first peak, which is downshifted to 1306 cm^{-1} , has decreased. The ten-minute growth shows an overall deviation from the spectrum intensity pattern. The intensity of the first peak increases, the intensity of the second peak decreases, and the intensity of the third peak decreases. The positions of these peaks relative to the run at 1 minute have stayed the same, however. The peak at 1980 cm^{-1} also appears in these three samples at approximately the same intensity.

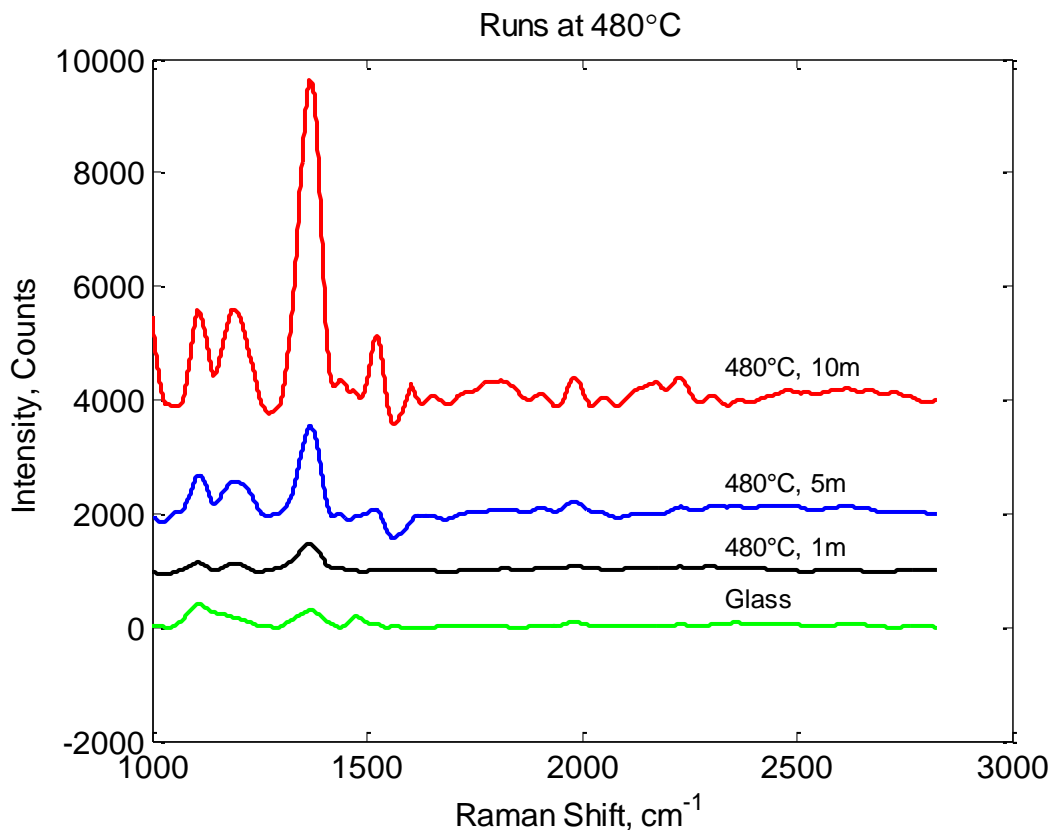


Figure 38: Raman spectra of runs performed at 480°C for 1 minute, 5 minutes, and 10 minutes as compared to blank glass.

The Raman spectra for samples grown at 480°C are shown above in Figure 38. For the 1 minute growth, three main peaks at 1107, 1192, and 1367 cm^{-1} appear. The peak at 1192 cm^{-1} appears in previous spectra as a shoulder to the first peak, however in these spectra it appears as a separate peak that does not experience a shift. The first peak does not undergo a shift from sample to sample either. For the 5 minute growth, a peak begins to appear at 1518 cm^{-1} that grows taller for the 10 minute growth, experiencing a slight shift to 1524 cm^{-1} . The peak at 1369 cm^{-1} grows more intense for both the 5 and 10 minute growths. Interestingly, the peak at 1980 cm^{-1} appears in all three samples and grows more intense with increasing growth time, a deviation from the three previous samples.

The Raman spectra can also be compared at the same temperatures but with increasing growth times. As shown below in Figure 39, the first peak at approximately 1110 cm^{-1} decreases with increasing temperature, however the shoulder of this peak develops and is intensified to form a second peak at 1192 cm^{-1} for the 480°C growth. The peak at 1374 cm^{-1} grows in intensity as temperature increases and is slightly downshifted to 1367 cm^{-1} at 480°C . Finally, the last main peak which starts at 1495 cm^{-1} decreases in intensity as temperature increases. It experiences an upshift to 1515 cm^{-1} at 380°C and disappears for the 480°C run. The peak at 1980 cm^{-1} decreases in intensity for increasing temperatures.

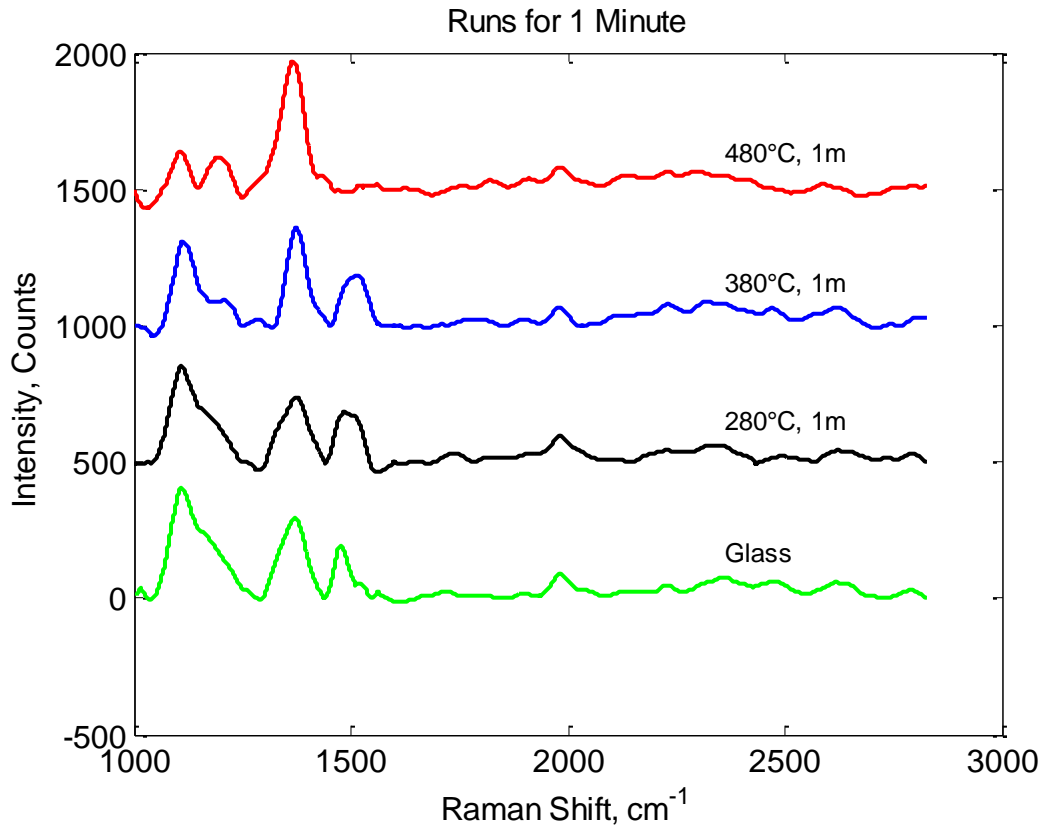


Figure 39: Raman spectra of runs performed for 1 minute at different temperatures.

The Raman spectra of growths performed for 5 minutes are shown below in Figure 40. At 280°C , all peaks are very low intensity, and the second main peak is almost nonexistent. However, as in Figure 39, the intensity of the second main peak around 1380 cm^{-1} increases with

increasing temperature. It also experiences a slight downshift from 1380 cm^{-1} at 380°C to 1370 cm^{-1} at 380°C . The intensity of the first main peak first decreases with increasing temperature at 380°C , then increases and the shoulder forms a separate peak at 1190 cm^{-1} for the run 480°C . The third main peak experiences an overall decrease in intensity and a slight upshift from 1506 cm^{-1} at 280°C to 1527 cm^{-1} at 380°C . At 480°C , this peak is very weak and has experienced a downshift to 1518 cm^{-1} . In opposition to runs performed for 1 minute, the intensity of the peak at 1980 cm^{-1} increases with increasing temperature.

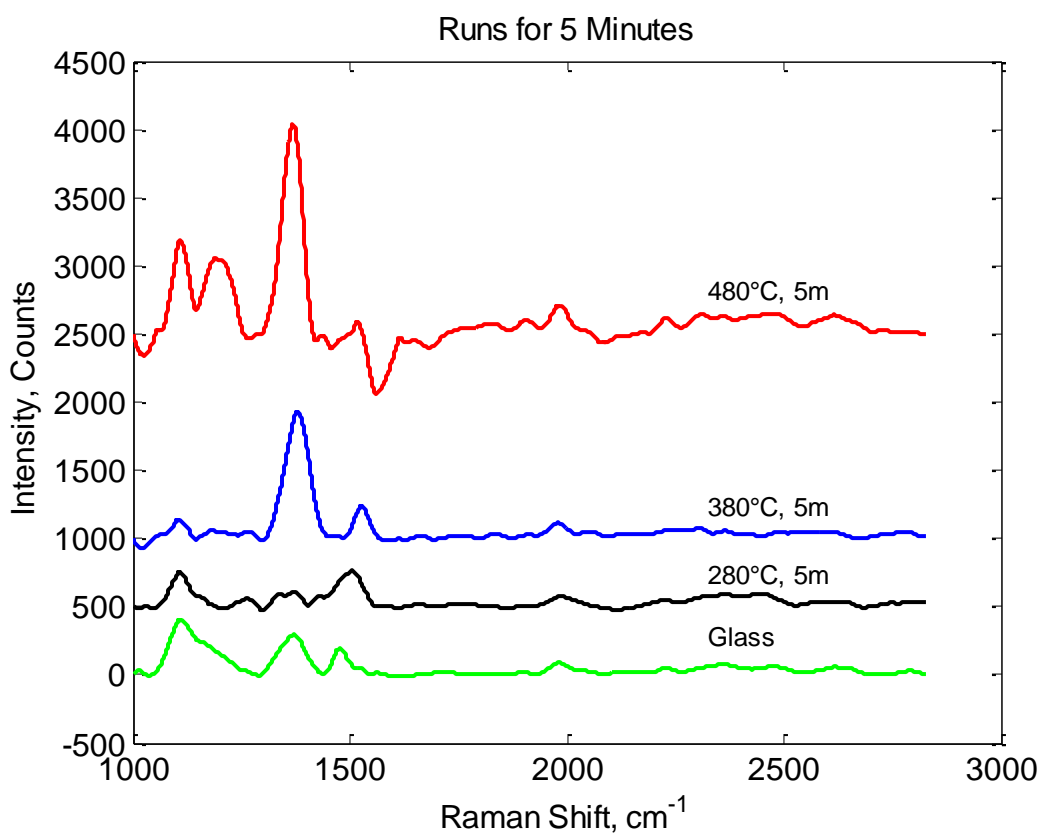


Figure 40: Raman spectra of runs performed for 5 minutes at different temperatures.

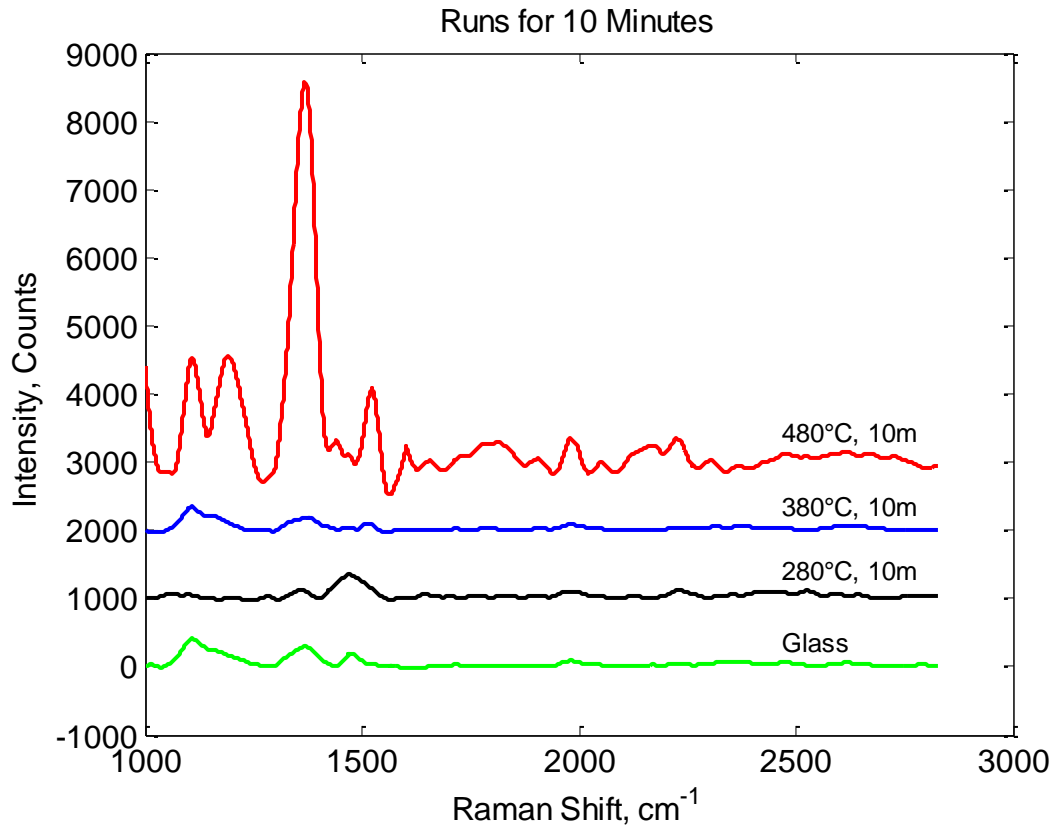


Figure 41: Raman spectra of runs performed for 10 minutes at different temperatures.

The Raman spectra of growths performed for 10 minutes are shown above in Figure 41. At 280°C, the peak at 1110 cm^{-1} is indistinguishable. The peak and its shoulder grow in intensity with increasing temperature and split into two separate peaks at 480°C. The second peak increases in intensity and experiences a slight upshift with increasing temperature. The third peak decreases in intensity and experiences an upshift from 280 to 380°C. From 380 to 480°C, however, it is found to increase in intensity and again experiences a slight upshift. The peak at 1980 cm^{-1} again increases in intensity.

A large overall trend is seen across these comparisons. In all cases, the Raman signal becomes more intense than the surrounding noise when the growth time and/or growth temperature are increased. Generally, higher temperatures and times led to more material being deposited, causing an amplification of the Raman signal. The second and third main peaks are

close in position to the known D and G peaks of graphite. The peak at 1980 cm^{-1} is clearly present in the spectrum of pure glass taken, however it does increase in intensity with increasing growth time and temperature.

4.3: Results of Scanning Electron Microscopy

SEM was used to investigate the deposition on copper from sample 6, run at 480°C for 5 minutes. Large flake-like structures were seen as shown in Figure 42. They varied in size and thickness, though most were approximately 500 nm in width. In Figure 42(a) areas with thin deposition were seen, and in Figure 42(b) a thicker formation is seen. Also seen in Figure 42(b) are areas with smaller flake-like structures, particularly in the lower portion of the image.

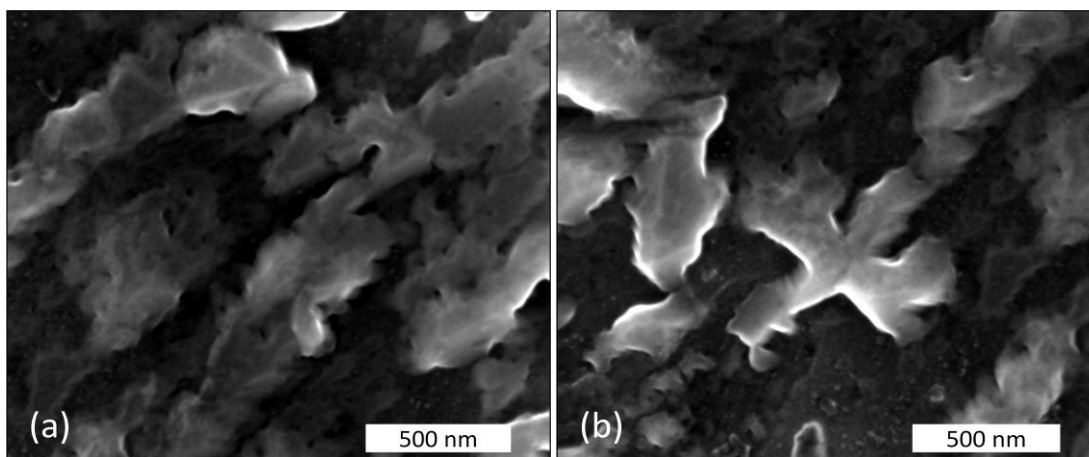


Figure 42: SEM imaging of large flake structures in sample 6.

SEM imaging was also performed on the copper substrate from sample 7, run at 480°C for 1 minute, as can be seen in Figure 43. Very small and some larger flake-like structures are also seen here. These structures also range in thickness and size. In both (a) and (b), a range of structure sizes and thicknesses are seen. Figure 43(a), a thick, large area of deposition is seen, along with many smaller surrounding flakes. In Figure 43(b), a few thinner areas are seen, as well as the smaller surrounding flakes.

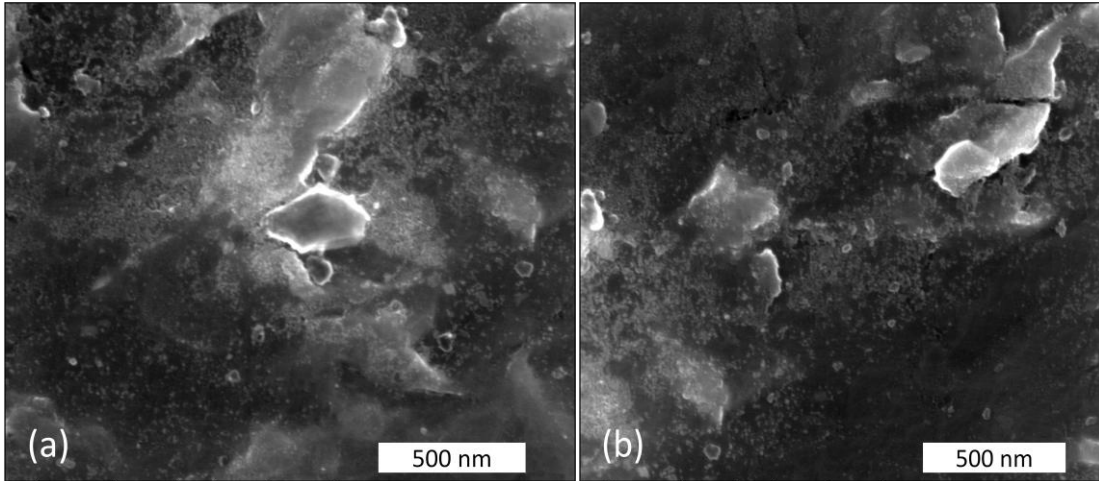


Figure 43: SEM imaging of flake-like structures in sample 7.

4.4: Results of Transmission Electron Microscopy

TEM imaging using a carbon-coated copper grid was also performed on sample 6. The results are shown below. Though spots with impurities were seen, the main structure seen was that of small circular formations. The images indicate a crystalline, multilayer flake-like structure of consistently less than 10 nm in diameter.

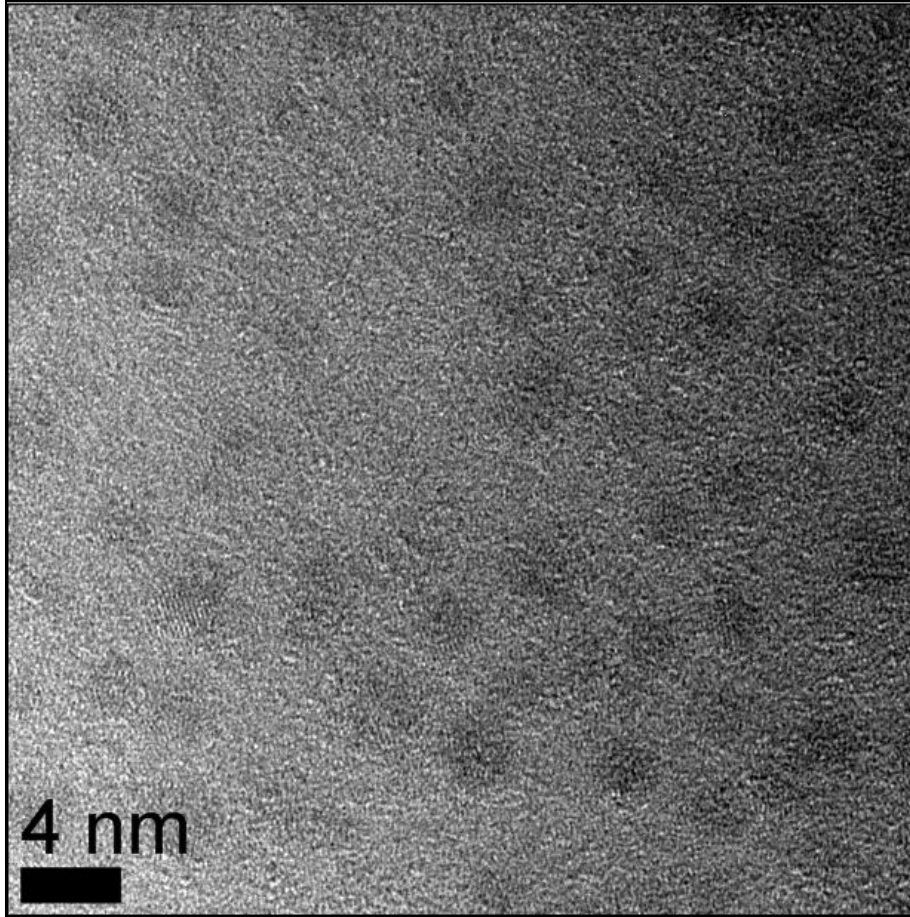


Figure 44: Multiple nanoflakes of varying diameter.

As seen above in Figure 44, small circular formations of crystalline material were common in the sample. The formations shown in this region are approximately 2 to 3 nanometers in diameter. These crystalline regions are mostly of singular orientation, though there do exist some places where multiple orientations exist.

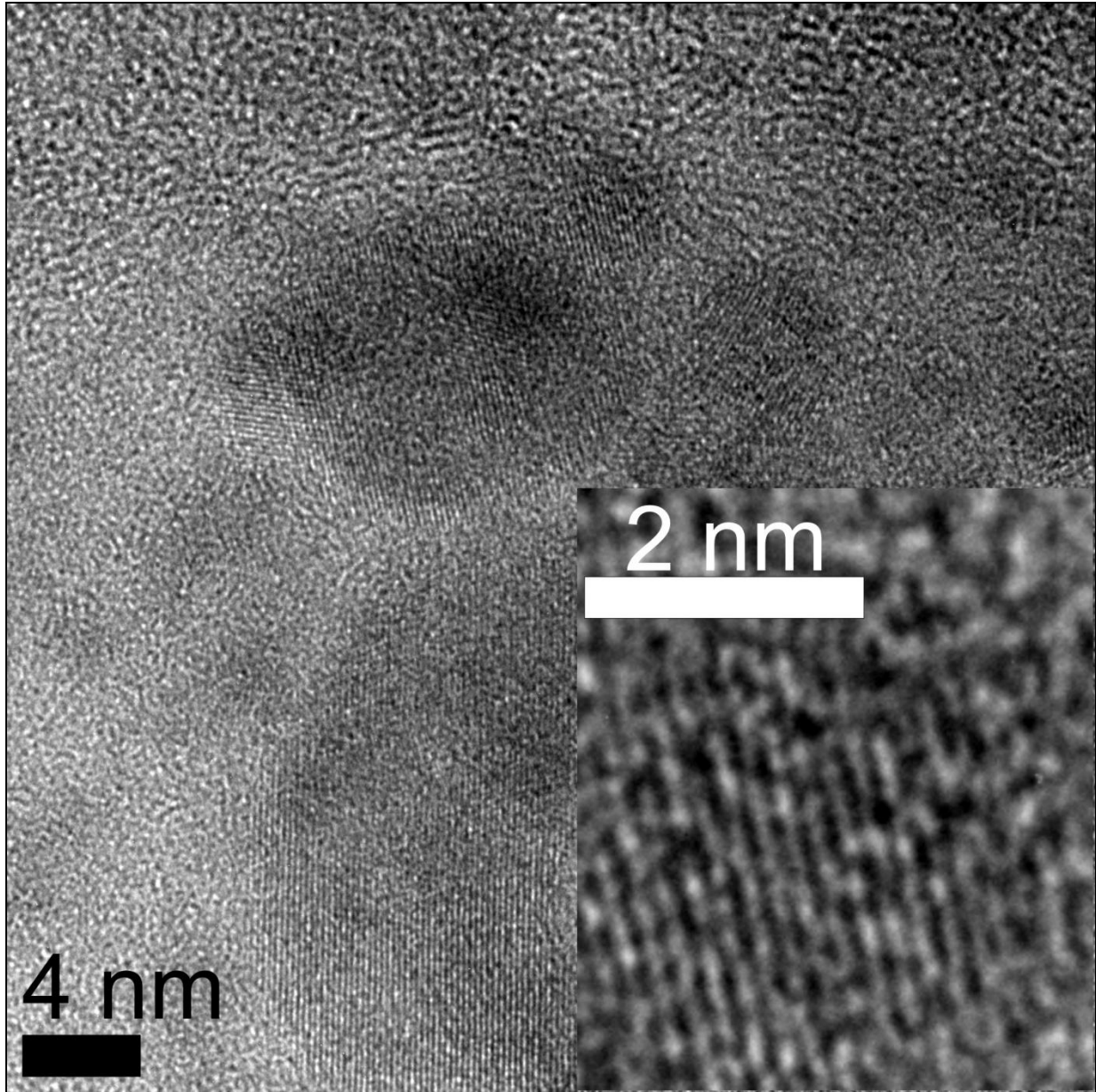


Figure 45: Larger nanoflakes showing a crystalline lattice.

In Figure 45, larger crystalline structures are seen. This image shows nanoflakes displaying multiple crystal orientations, as can be seen in the top flake-like formation. It is possible that the structures in the photographs in Figure 44 and Figure 45 are not individual pieces and instead one continuous layer. If the flake were one layer, any bending or folding of

the material could exhibit a non-crystalline area and therefore would not be shown in TEM analysis.

When visualizing graphene using TEM, one can estimate the lattice parameters by looking at the “holes” in the hexagonal lattice – that is, the center of the lattice where no carbon atom is present. As can be seen in Figure 46, the blank spaces in the lattice are easily visualized using TEM, even if the individual carbon atoms are more difficult to see. Using the “blank spaces” in the crystal lattice as represented in Figure 47, we can calculate the distance between the rows of carbon to be approximately 2.1 Å, as indicated in Figure 47 and Figure 48. This corresponds with the spacing of a graphene lattice. However, this is also close to the spacing of the diamond structure.

Energy dispersive X-ray spectroscopy, or EDX, was performed on these spots, the results of which are shown in Figure 49. Small signals from nickel and silicon contaminants are seen. The main element in these structures is carbon, however, confirming the presence of few-layer graphitic nanoflakes.

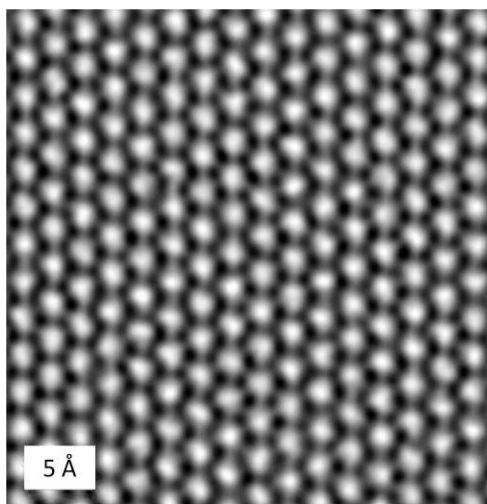


Figure 46: Image showing “holes” or “blank spaces” in the graphene lattice [49].

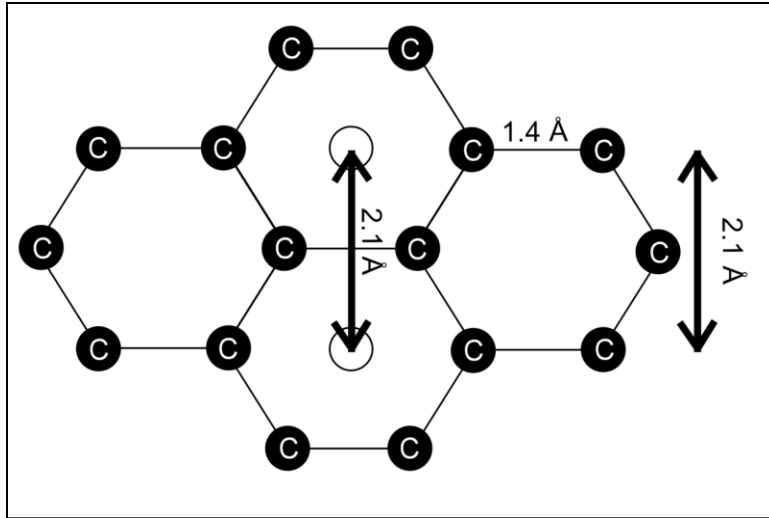


Figure 47: Graphical representation of “blank space” in the lattice corresponding to TEM imaging.

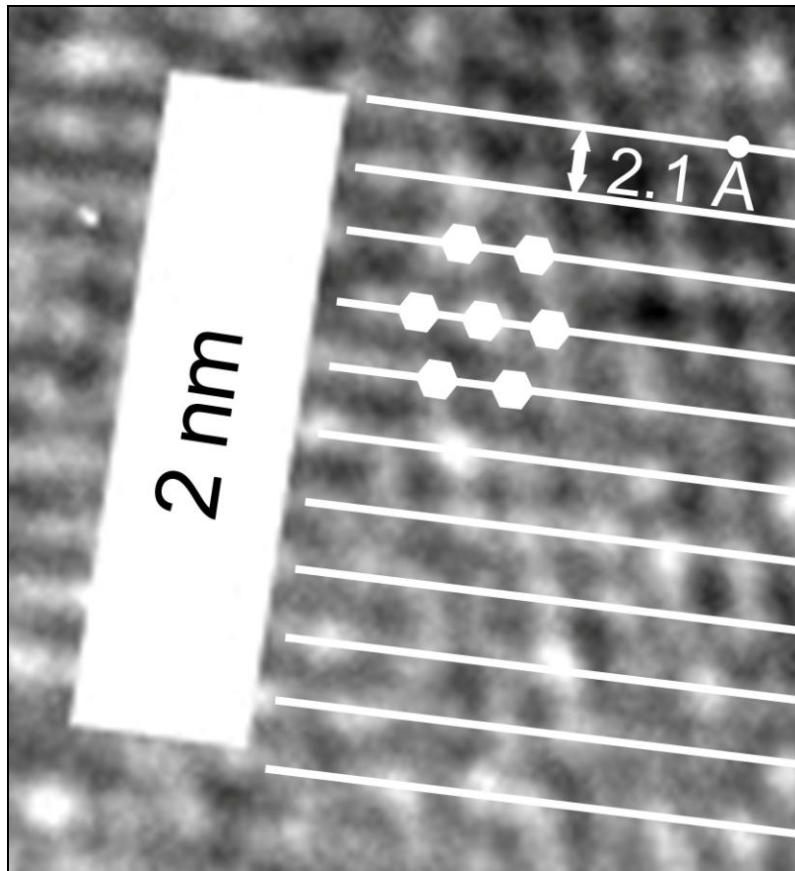


Figure 48: Zoomed-in image of graphene planes showing the “blank space” spacing.

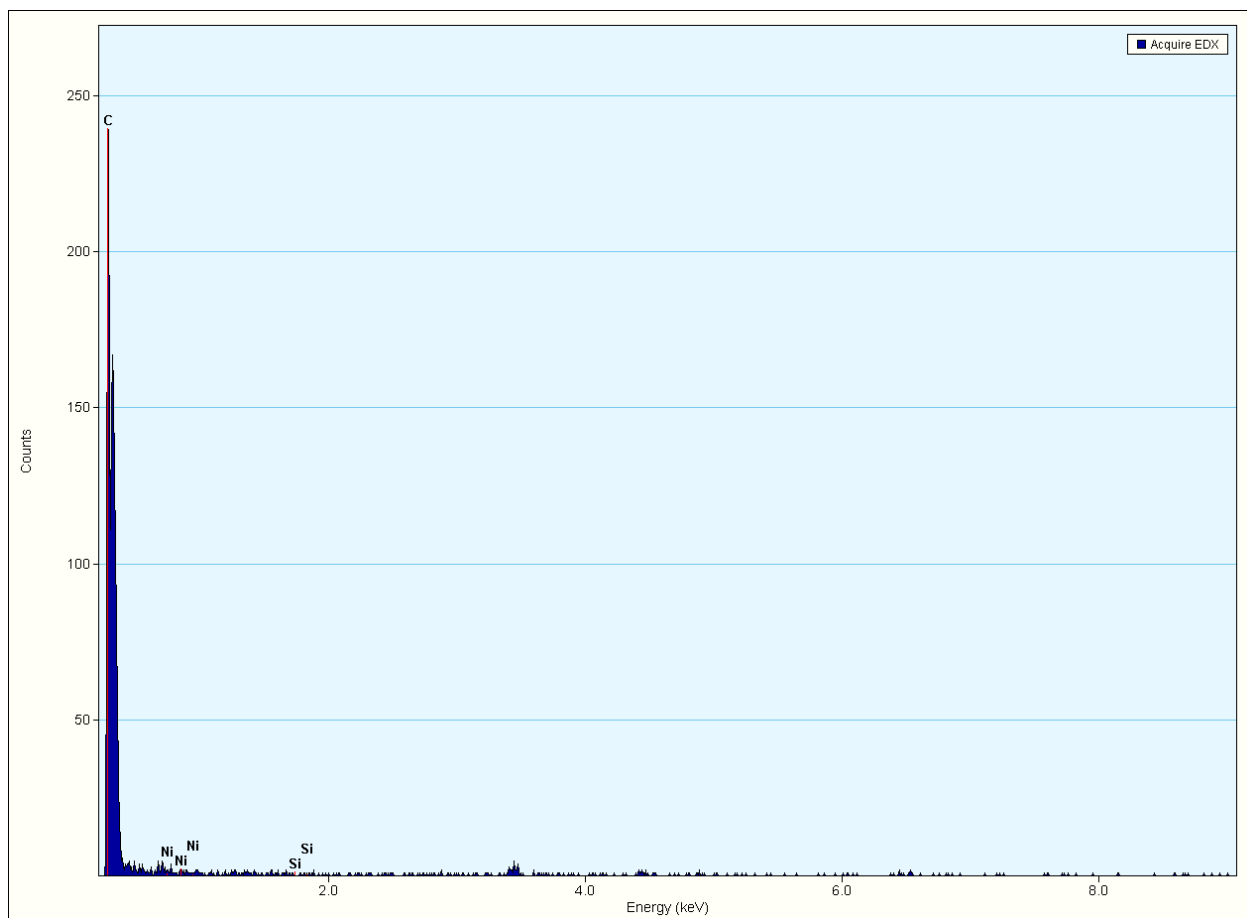


Figure 49: EDX analysis of nanoflakes.

Chapter 5: Conclusion and Future Work

In this thesis, a thorough review of research focused on low-temperature chemical vapor deposition synthesis of graphene was given, detailed in Chapter 2. It is seen that growth at low temperatures relies on plasma enhancement for carbon deposition. The growth time and temperature parameters also play key roles in the deposition process. Therefore, a series of experiments varying temperature and time was designed and executed, as detailed in Chapter 3. In addition to these experiments, an advanced ultra-high vacuum plasma-enhanced chemical vapor deposition (UHV-PECVD) machine described in Chapter 3 was designed and built by a team of students, post-docs, professors, and staff. The uniqueness and advanced abilities of this system will allow the University of Arkansas access to cutting-edge research in the field of nanotechnology. Specific aspects of the UHV-PECVD system, including the dual manual and computer control systems and the alarm systems, were designed and built with ease of use and safety as top priorities at all times.

The films produced from the growth experiments were characterized by optical transmittance, Raman spectroscopy, scanning electron microscopy, and transmission electron microscopy. From the data gathered and presented, it is evident that a nanoscale, crystalline form of graphitic carbon film was deposited. The Raman spectra do not implicitly indicate the presence of graphene. The intensity of the majority of Raman spectra was comparable to the intensity of the signal from the blank glass. However, the slight change in the peak positions indicates a film present. In thicker samples, such as samples 1 and 6 both grown at 480°C for 10 and 5 minutes respectively, the Raman intensity is much higher than that of glass. The peak at approximately 1370 cm^{-1} is much more intense. This peak is close to the known D peak of graphene, the disorder peak. One of the main contributors to the D peak, as stated earlier, is an edge. As indicated by TEM and SEM photos, nanoscale flake-like structures were seen instead of

one continuous film. The images would therefore support the Raman spectra. The intensity of the third main Raman peak is close to the G peak of graphite, pointing to a carbon film present. Optical transmittance data do not indicate a single- or multi-layer graphene structure, as the measured transmittance loss do not exactly correspond to a multiple of the known constant of 2.3% [18]. In thicker samples, however, it was seen that a higher percentage of transmittance was lost. Therefore, the structure present is absorbing light in the visible region. The samples may have some amorphous carbon formation as well as crystalline nanoflakes.

From the data presented, it is evident that though single-layer graphene growth was not achieved, fine-tuning the growth parameters would increase the possibility of graphene growth. Higher temperature and higher plasma power could provide more energy for sp^2 bond formation, leading to more growth. The ratio of hydrogen to methane could be increased so that the process of hydrogen removal occurring at the metal substrate surface is enhanced. These parameters could be investigated on the UHV-PECVD system.

Fine-tuning the graphene growth process to produce high-quality films can be accomplished using the new UHV-PECVD system. Investigating the parameter space specifically at low temperatures is the key to forming a device-oriented process. Other types of depositions could be implemented along with graphene growth to produce devices. Facilities such as the HiDEC could be used for graphene patterning. Analysis on substrate effects at lower temperatures could also be performed. Therefore, depositions will be repeated using the UHV-PECVD system, and the parameter space can be expanded based on the system's cutting-edge capabilities. Data across the two systems can be compared to further knowledge of the growth process.

Graphene, what some are calling the “new silicon”, has a wealth of potential applications across the electronic, biomedical, and nanoscale technologies. The possibilities for its use are endless, and therefore, graphene research is essential to bringing the University of Arkansas to the forefront of tomorrow’s technology. The UHV-PECVD system and these preliminary carbon depositions have brought this university one step closer to advanced technological innovation.

References

- [1] K. S. Novoselov et al., "Electric Field Effect in Atomically Thin Carbon Films," *Science*, vol. 306, pp. 666-669, October 2004.
- [2] A. K. Geim and K. S. Novoselov, "The Rise of Graphene," *Nature Materials*, vol. 6, pp. 183-191, March 2007.
- [3] K. S. Novoselov et al., "Two-dimensional gas of massless Dirac fermions in graphene," *Nature*, vol. 438, pp. 197-200, November 2005.
- [4] A. K.M. Newaz, Yevgeniy S. Puzyrev, Bin Wang, Sokrates T. Pantelides, and Kirill I. Bolotin, "Probing Charge Scattering Mechanisms in Suspended Graphene by Varying Its Dielectric Environment," *Nature Communications*, pp. 1-6, March 2012.
- [5] Qingkai Yu et al., "Graphene segregated on Ni surfaces and transferred to insulators," *Applied Physics Letters*, vol. 93, no. 113103, 2008.
- [6] Congqin Miao, Churan Zheng, Owen Liang, and Ya-Hong Xie, "Chemical Vapor Deposition of Graphene," in *Physics and Applications of Graphene - Experiments*, Sergey Mikhailov, Ed. Croatia: InTech, 2011, ch. 3, pp. 37-54.
- [7] Andrea C. Ferrari, "Raman spectroscopy of graphene and graphite: Disorder, electron-phonon coupling, doping and nonadiabatic effects," *Solid State Communications*, vol. 143, pp. 47-57, 2007.
- [8] Dieter K. Schroder, *Semiconductor Material and Device Characterization*, 3rd ed. Hoboken, United States of America: John Wiley & Sons, Inc, 2006.
- [9] Akio Yoshimori and Yoshiharu Kitano, "Theory of the Lattice Vibration of Graphene," *Journal of the Physical Society of Japan*, vol. 11, no. 4, pp. 352-361, 1956.
- [10] F. Tuinstra and J. L. Koenig, "Raman Spectrum of Graphite," *Journal of Chemical Physics*, vol. 53, no. 3, pp. 1126-1130, August 1970.
- [11] Horiba Scientific. (2011) Application Note: Perspectives on Raman Spectroscopy of Graphene. [Online]. <http://www.horiba.com/scientific/products/raman-spectroscopy/applications/application-notes-articles/>
- [12] A. C. Ferrari et al., "Raman Spectrum of Graphene and Graphene Layers," *Physical Review Letters*, vol. 97, p. 187401, November 2006.
- [13] Zhenhua Ni, Yingying Wang, Ting Yu, and Zexiang Shen, "Raman Spectroscopy and Imaging of Graphene," *Nano Research*, vol. 1, pp. 273-291, 2008.

- [14] FEI Company. (2012) Magellan XHR Scanning Electron Microscope (SEM). [Online]. <http://www.fei.com/products/scanning-electron-microscopes/magellan.aspx>
- [15] Encyclopædia Britannica Online. (2008) Scanning Electron Microscope. [Online]. <http://www.britannica.com/EBchecked/media/110970/Scanning-electron-microscope>
- [16] FEI Company. (2012) Titan Transmission Electron Microscope (TEM). [Online]. <http://www.fei.com/products/transmission-electron-microscopes/titan.aspx>
- [17] Encyclopædia Britannica Online. (2008) Transmission Electron Microscope (TEM) (Instrument). [Online]. <http://www.britannica.com/EBchecked/topic/602949/transmission-electron-microscope-TEM/>
- [18] R. R. Nair et al., "Fine Structure Constant Defines Visual Transparency of Graphene," *Science*, vol. 320, p. 1308, June 2008.
- [19] Yasumitsu Miyata et al., "A Simple Alcohol-Chemical Vapor Deposition Synthesis of Single-Layer Graphenes Using Flash Cooling," *Applied Physics Letters*, vol. 96, pp. 263105-263107, 2010.
- [20] Xuesong Li et al., "Large-Area Synthesis of High-Quality and Uniform Graphene Films on Copper Foils," *Science*, vol. 324, pp. 1312-1314, June 2009.
- [21] Seung Jin Chae et al., "Synthesis of Large-Area Graphene Layers on Poly-Nickel Substrate by Chemical Vapor Deposition Wrinkle Formation," *Advanced Materials*, vol. 21, pp. 2328-2333, 2009.
- [22] Jianjun Wang et al., "Synthesis of Carbon Nanosheets by Inductively Coupled Radio-Frequency Plasma Enhanced Chemical Vapor Deposition," *Carbon*, vol. 42, pp. 2867-2872, 2004.
- [23] Mingyao Zhu et al., "A Mechanism for Carbon Nanosheet Formation," *Carbon*, vol. 45, pp. 2229-2234, 2007.
- [24] Mingyao Zhu et al., "Synthesis of Carbon Nanosheets and Carbon Nanotubes by Radio Frequency Plasma Enhanced Chemical Vapor Deposition," *Diamond and Related Materials*, vol. 16, pp. 196-201, 2007.
- [25] Alexander Malesev et al., "Synthesis of Few-Layer Graphene via Microwave Plasma-Enhanced Chemical Vapor Deposition," *Nanotechnology*, vol. 19, pp. 1-6, 2008.
- [26] G. D. Yuan et al., "Graphene Sheets via Microwave Chemical Vapor Deposition," *Chemical Physics Letters*, vol. 467, pp. 361-364, 2009.

- [27] M. Hiramatsu, K. Shiji, H. Amano, and M. Hori, "Fabrication of Vertically Aligned Carbon Nanowalls Using Capacitively Coupled Plasma-Enhanced Chemical Vapor Deposition Assisted by Hydrogen Radical Injection," *Applied Physics Letters*, vol. 84, pp. 4708-4710, June 2004.
- [28] Gopichand Nandamuri, Sergei Roumimov, and Raj Solanki, "Remote Plasma Assisted Growth of Graphene Films," *Applied Physics Letters*, vol. 96, pp. 154101-1 - 154101-3, 2010.
- [29] Y. Kim et al., "Low-Temperature Synthesis of Graphene on Nickel Foil by Microwave Plasma Chemical Vapor Deposition," *Applied Physics Letters*, vol. 98, pp. 263106-236108, 2011.
- [30] Jaeho Kim et al., "Low-Temperature Synthesis of Large-Area Graphene-Based Transparent Conductive Films Using Surface Wave Plasma Chemical Vapor Deposition," *Applied Physics Letters*, vol. 98, pp. 091502-1 - 091502-3, 2011.
- [31] Takatoshi Yamada, Masatou Ishihara, Jaeho Kim, Masataka Hasegawa, and Sumio Ijima, "A Roll-to-Roll Microwave Plasma Chemical Vapor Deposition Process for the Production of 294 mm Width Graphene Films at Low Temperature," *Carbon*, vol. 50, pp. 2615-2619, 2012.
- [32] Eun Sung Kim et al., "Low-Temperature Graphene Growth Using Epochal Catalyst of PdCo Alloy," *Applied Physics Letters*, vol. 99, pp. 223102-1 - 223102-3, 2011.
- [33] Lam Van Nang and Eui-Tae Kim, "Controllable Synthesis of High-Quality Graphene Using Inductively-Coupled Plasma Chemical Vapor Deposition," *Journal of the Electrochemical Society*, vol. 159, no. 4, pp. K93-K96, 2012.
- [34] A. Kumar, A. A. Voevodin, D. Zemlyanov, D. N. Zakharov, and T. S. Fisher, "Rapid Synthesis of Few-Layer Graphene Over Cu Foil," *Carbon*, vol. 50, pp. 1546-1553, 2012.
- [35] Albert Dato, Velimir Radmilovic, Zonghoon Lee, Jonathan Phillips, and Michael Frenklach, "Substrate-Free Gas-Phase Synthesis of Graphene Sheets," *Nano Letters*, vol. 8, no. 7, pp. 2012-2016, 2008.
- [36] Edwards Vacuum, Instruction Manual: XDS Dry Pump, 2010.
- [37] Pfeiffer Vacuum, Turbomolecular Drag Pump with Magnetic Bearings, 2010.
- [38] Benjamin Conley, Design and Construction of an Ultra High Vacuum Chemical Vapor Deposition for Group IV Material Growth, 2011, Master's thesis.
- [39] Edwards Vacuum, Instruction Manual: QDP Drystar Vacuum Pumps, 2000.

- [40] Edwards Vacuum, Instruction Manual: STP Series Turbomolecular Pumps, 2008.
- [41] Sumitomo (SHI) Cryogenics of America, Marathon CP-8 Cryopump Technical Manual, 2008.
- [42] Pfeiffer Vacuum, Operating Instructions: Compact FullRange Gauge, 2008.
- [43] A. Ellett and R. M. Zabel, "The Pirani Gauge for the Measurement of Small Changes of Pressure," *Physical Review*, vol. 37, pp. 1102-1111, May 1931.
- [44] Pfeiffer Vacuum. (2012) Indirect, Gas-Dependent Pressure Measurement. [Online]. <http://www.pfeiffer-vacuum.com/know-how/vacuum-measuring-equipment/fundamentals-of-total-pressure-measurement/indirect-gas-dependent-pressure-measurement/technology.action?chapter=tec3.1.2>
- [45] MKS. (2011) How an MKS Baratron Capacitance Manometer Works. [Online]. <http://www.mksinst.com/docs/UR/barainfo2b.aspx>
- [46] Paul Ray Moffitt, Study of VHF Deposited Amorphous Germanium and Amorphous Germanium Carbon Alloy for Multijunction Solar Cells, 1996, Doctoral Dissertation.
- [47] D Manara, A Grandjean, and D R Neuville, "Advances in Understanding the Structure of Borosilicate Glass: A Raman Spectroscopy Study," *American Mineralogist*, vol. 94, pp. 777-784, 2009.
- [48] A. C. Ferrari and J. Robertson, "Interpretation of Raman Spectra of Disordered and Amorphous Carbon," *Physical Review B*, vol. 61, no. 20, pp. 14095-14107, 2000.
- [49] Xiaodong Xu. (2011) Xu Group: Nanoscale Optoelectronics Laboratory. [Online]. <http://faculty.washington.edu/xuxd/research-optoelectronics.html>

